J. Mech. Phys. Solids 152 (2021) 104407

Contents lists available at ScienceDirect

Journal of the Mechanics and Physics of Solids

journal homepage: www.elsevier.com/locate/jmps

Customized broadband pentamode metamaterials by topology optimization

Hao-Wen Dong [a,b], Sheng-Dong Zhao [e], Xuan-Bo Miao [c], Chen Shen [f], Xiangdong Zhang [g], Zhigao Zhao [g], Chuanzeng Zhang [h], Yue-Sheng Wang [c,d,*], Li Cheng [b,**]

[a] Institute of Advanced Structure Technology, Beijing Institute of Technology, Beijing 100081, China
[b] Department of Mechanical Engineering, The Hong Kong Polytechnic University, Hong Kong, China
[c] Department of Mechanics, School of Mechanical Engineering, Tianjin University, Tianjin 300350, China
[d] Institute of Engineering Mechanics, Beijing Jiaotong University, Beijing 100044, China
[e] School of Mathematics and Statistics, Qingdao University, Qingdao 266071, China
[f] Department of Mechanical Engineering, Rowan University, Glassboro, NJ 08028, USA
[g] Wuhan Second Ship Design and Research Institute, Wuhan 430064, China
[h] Department of Civil Engineering, University of Siegen, Siegen D-57068, Germany

ARTICLE INFO

Keywords:
Pentamode
Topology optimization
Single-mode
Broadband
Anisotropy
Metasurfaces
Evanescent surface mode

ABSTRACT

Pentamode metamaterials (PMs), a kind of metafluids composed of complex solid medium, have shown enormous potential for both elastic wave and underwater acoustic wave manipulation. However, due to the lack of thorough understanding of the formation mechanism, most reported artificial and empirical PMs share very similar topological features, thus depriving the possibility of obtaining rigorous combination of wave parameters that are required to deliver desirable and prescribed properties and functionalities. To tackle this challenge, with the assumption of C_{2v}, C_{4v} and C_{6v} symmetries in both square and triangle lattices, we propose a unified inverse strategy to systematically design and explore a series of novel isotropic or anisotropic PM microstructures through bottom-up topology optimization. Optimized PM microstructures are designed to provide customized effective mass density, elastic modulus, anisotropy degree and pentamode features on demand. We demonstrate that most optimized microstructures possess broadband single-mode range of exclusive longitudinal waves; some even feature record-breaking relative single-mode bandwidths exceeding 150%. Upon shielding lights on the beneficial topological features of the broadband PMs, we extract the main topological features to form simplified PM configurations, i.e., multiple symmetric solid blocks with slender rods, which can induce the multiform multiple-order rotational vibrations or the integration of the low-order rotational vibrations and anisotropic local resonances for the broadband single-mode nature. At a higher design level, we establish a dedicated inverse-design strategy, under the function-macrostructure-microstructure paradigm, to conceive a novel broadband subwavelength underwater pentamode shielding device, which enables the conversion of propagating acoustic wave to the evanescent surface wave mode within the frequency range [1000 Hz, 4000 Hz]. Our study offers new possibilities for the practical realization of broadband PMs and underwater pentamode devices with rigorously

* Corresponding author at: Department of Mechanics, School of Mechanical Engineering, Tianjin University, Tianjin 300350, China.
** Corresponding author.
E-mail addresses: yswang@tju.edu.cn (Y.-S. Wang), li.cheng@polyu.edu.hk (L. Cheng).

https://doi.org/10.1016/j.jmps.2021.104407
Received 4 October 2020; Received in revised form 1 February 2021; Accepted 18 March 2021
Available online 20 March 2021

tailored effective parameters, thus bring the PM-based technology within reach for practical applications.

1. Introduction

Metamaterials (Pendry, 2000; Liu et al., 2000; Smith et al., 2004; Zheludev et al., 2012), artificially engineered composite materials/structures, can enable many fascinating and designable physical properties which are difficult, if not impossible, to be achieved by nature materials. The rapid development made during the past several decades allowed the exploration of new capabilities and application territories which show great promise for designing brand-new, high-efficiency, multifunctional and integrated functional devices in optical (Shalaev et al., 2007; Jahani et al., 2016), acoustic (Fang et al., 2006; Cummer et al., 2016), mechanical (Liu et al., 2000; Wu et al., 2011; Lai et al., 2011; Zhu et al., 2014; Coulais et al., 2017; Frenzel et al., 2017) and thermal (Liu et al., 2011; Davis et al., 2014; Li et al., 2019) fields. Due to the specific resonance mechanisms, most metamaterials possess zero (Nguyen et al., 2010; Moitra et al., 2013; Li et al., 2015), single negative (Fang et al., 2006; Poddubny et al., 2013; Shen et al., 2015; Dong et al., 2018) or double negative (Wu et al., 2011; Liang et al., 2012; Yang et al., 2013; Lai et al., 2011; Zhu et al., 2014; Dong et al., 2017, 2019, 2020) effective constitutive parameters. However, the inherent and inevitable energy loss originated from the resonances in these metamaterials is seen to be a bottlenecking factor hampering the realization of broadband properties. Alternatively, capitalizing on factors such as non-resonance, low and wide frequency range, solid form and possible strong anisotropy, pentamode metamaterials (PMs) (Milton and Cherkaev, 1995; Norris 2008; Kadic et al., 2012) emerge as a new category of solid metamaterials with positive constitutive parameters, which can, in principle, can possess five zero and one nonzero eigenvalues to only bear the compressive deformation. In this sense, PMs can also be referred to as “metafluids”, conducive to applications such as elasto-mechanical cloaking (Bückmann et al., 2014), ultrasound imaging (Hladky-Hennion et al., 2013), underwater acoustic control (Layman et al., 2013; Tian et al., 2015) and elastic mode conversion (Zheng et al., 2019). More interestingly, uniting PMs and the transformation acoustics (Norris 2008), graded distributions or metasurfaces allows the design of underwater cloaking equipment (Chen et al., 2015, 2017; Chen et al., 2018; Sun et al., 2019) of high practicability.

With specific and artificially designed topologies, several PMs and related acoustic devices show their potential in static and dynamic applications. So far, structural features of the reported PMs are mainly honeycomb-lattice for 2D and diamond-lattice double-cone for 3D systems. For static applications, conventional PM microstructures root in creating point contact to produce infinitesimal shear modulus, which inevitably makes the PM very instable and impractical. In 2012, researchers (Kadic et al., 2012) firstly employed the direct-laser-writing technology to manufacture microscopic 3D polymer PMs with small finite connection diameters, leading to a ratio of bulk modulus to shear modulus as high as 1000. Then, by taking advantage of the scalability of continuum mechanics, several macroscopic 3D PMs were developed, fabricated and tested (Schittny et al., 2013) with excellent elastic properties demonstrated. Using metallic materials, acceptable energy dissipation was confirmed by the post-elastic response (Amendola et al., 2016). Due to the ease in modulating their effective parameters, 3D polymer PMs can also be adopted to design an approximate elasto-mechanical core-shell cloak in millimeter scale (Bückmann et al., 2014). In general, most periodic porous lattice structures with large slenderness ratios can be regarded as PMs. For typical pentamode lattices, it is useful to predict the effective parameters through analytical expressions for both isotropic and anisotropic systems (Norris 2014). In particular, PMs can be further designed as auxetic metamaterials for energy absorption and fracture resistance. Changing the connection size of 3D diamond-lattice double-cone PM can enable a transition of an anti-auxetic metamaterial to an auxetic one (Kadic et al., 2013).

Benefiting from the arbitrarily designable effective elastic tensor, PM can be artificially and tactically designed to achieve different types of acoustic and elastic wave manipulation and functionalities, including low-frequency wave attenuation (Krushynska et al., 2018), negative refraction (Hladky-Hennion et al., 2013; Tian et al., 2015), underwater imaging (Hladky-Hennion et al., 2013; Tian et al., 2015; Su et al., 2017), acoustic mirage (Layman et al., 2013), non-diffractive Bessel beam (Tian et al., 2015), underwater acoustic bend (Sun et al., 2018), wave-type conversion (Chen and Hu, 2019; Zheng et al., 2019), asymmetric propagation (Chu et al., 2020), underwater annular cloak (Scandrett et al., 2011; Chen et al., 2017), carpet cloaks (Chen et al., 2018; Sun et al., 2019) and even topologically protected propagation of elastic waves (Guo et al., 2017), etc. In 2013, using 2D oblique honeycomb-lattice structures, Laymen et al. firstly combined the concepts of microstructural design and wave functionality to achieve highly anisotropic PM microstructures for conceiving acoustic mirage devices (Layman et al., 2013). Subsequently, similar highly symmetric honeycomb-lattice structures were demonstrated to possess negative group velocity in high-frequency range (Hladky-Hennion et al., 2013) and ideally mimic water in acoustic properties as well (Zhao et al., 2017). In addition, the gradient-indexed underwater lens based on honeycomb-lattice PMs can effectively realize broadband focusing within [20 kHz, 40 kHz] in a back-scattering-free manner (Su et al., 2017). Similar 2D honeycomb-lattice PMs with symmetrically distributed rectangular blocks can be assembled to ensure the ideal impedance matching between underwater acoustic bend and water. If controllable high anisotropy can be introduced into the honeycomb-lattice PMs, 2D broadband annular invisible cloak can be realized for underwater acoustic applications (Chen et al., 2017). However, for the carpet cloak, the traditional linear transformation method should be changed as the quasi-conformal transformation for a 2D acoustic carpet cloak with the honeycomb-lattice PMs (Sun et al., 2019). As for its 3D counterpart, Scandrett et al. analytically discovered that 3D anisotropic PMs can achieve good broadband cloaking by using only a few layers (Scandrett et al., 2011), thus reconfirming the appealing value of the anisotropic pentamode feature. The broadband single-mode behavior within a 3D diamond-lattice double-cone PM was found from the band structures (Martin et al., 2012). By introducing laminate configuration, 3D PMs with independently tailored effective elastic modulus and mass density were shown to be feasible (Kadic et al., 2014). When

combing the stiffeners (Fraternali and Amendola, 2017) or phononic plates (Krushynska et al., 2018) with pentamode units, it is possible to achieve low-frequency wave attenuation or impact protection, respectively. Previous studies showed that the mechanical and acoustic properties of representative PMs are sensitive to the structural parameters (Cai et al., 2016) and anisotropy degree (Cai et al., 2020). Recently, it was shown that topology optimization based on elasticity tensor and microstructural symmetries can realize static microstructures in the rectangular lattice for a target pentamode tensor by using the prescribed initial geometry conditions (Podestá et al., 2019). Inspired by similar crystal symmetry, topology optimization of only minimizing the effective static shear modulus (Year et al., 2020) also generated three isotropic pentamode microstructures.

Upon achieving perfect matching with water, PMs are ideal candidates to be used as the basic building blocks for conceiving underwater acoustic metasurfaces as well. In recent years, different combinations of 2D honeycomb-lattice microstructures and phase gradients have been proposed to cater for particular underwater acoustic functionalities, such as the negative refraction (Tian et al., 2015), focusing (Tian et al., 2015), asymmetric transmission (Chu et al., 2020), mode conversion (Chen and Hu, 2019) and carpet cloak (Chen et al., 2018), etc. Moreover, some peculiar anisotropic PMs can also be utilized to create singly polarized solids carrying only shear waves (Zheng et al., 2019). However, most reported PM metasurfaces adopted very similar honeycomb-lattice topology, which limits the performance and impedes the exploration of new underlying mechanisms or new extreme functionalities using PM metasurfaces.

Up to now, several apparent challenges remain, which impede the practical applications of PMs. (1) Only few microstructural forms are available, mostly honeycomb-lattice topologies and diamond-lattice double-cone ones for 2D and 3D systems, respectively. This apparently leaves a huge space to explore more novel microstructures. (2) Limited by the intuitive and empirical nature of the reported design approaches, no explicit design method can directly generate broadband single-mode frequency range of interest. (3) Systematic comparisons between the commonly used square- and triangle-lattice systems are lacking. (4) There is also a lack of understanding on the mechanism of broadband single-mode wave motion underpinning pentamode features. (5) As one of the main applications of PMs, an underwater acoustic cloak has to cover entire object, thus calling for a simpler PM device with distinctly different cloaking mechanisms. In summary, for truly feasible and practical PM devices, a crucial step is to develop a unified and universal design paradigm to realize customized PM designs with arbitrarily prescribed effective elasticity tensor and wave properties on demand. Because of the multiple parameters involved and the extreme mechanical properties required, a systematic inverse design will be a challenging classic non-convex, massive-variable and multi-constrained optimization problem.

In this paper, a unified and versatile inverse-design strategy for PMs is proposed. We firstly construct the topology optimization of PM microstructures by introducing effective mass density, effective longitudinal and shear moduli, anisotropy degree and impedance matching extent simultaneously for the prescribed C_{2v}-, C_{4v}- and C_{6v}-symmetry microstructures in both square- and triangle-lattice systems. Systematic optimizations lead to a series of PM microstructures with customized wave properties, including (1) free isotropic PMs; (2) broadband isotropic or anisotropic PMs with single mode and impedance matching; (3) anisotropic PMs with prescribed anisotropy; and (4) anisotropic PMs with impedance matching and prescribed anisotropy. Most optimized PMs can give rise to broadband single-mode frequency ranges whose relative bandwidths are larger than 100%. The relative bandwidths of two customized triangle-lattice PMs can even exceed 150%. Moreover, inspired by the inverse-designed microstructures, we extract the main topological features and propose simplified square- and triangle-lattice PM configurations. To further conceive underwater metamaterials exhibiting exceptional wave properties, we develop an integrated inverse-design strategy, sequentially encompassing the prescribed functionality, macrostructures and PM microstructures, to realize a broadband subwavelength underwater shielding device within an ultra-broadband frequency range [1000 Hz, 4000 Hz]. We numerically demonstrate that the customized device can convert the incident propagating acoustic wave to the evanescent surface mode within the prescribed broad subwavelength range. The comprehensive solution package presented here, including the systematic inverse-design approach, achieved specific topological features, revealed broadband single-mode mechanisms and customized broadband acoustic device, collectively contributes to the state-of-the-art of PMs and offers a pivotal transition from the conceptual design to the large-scale applications of PMs.

This paper is organized as follows. Section 2 presents the basic wave equations for the general periodic elastic structures, characterization of effective intrinsic parameters and wave responses of pentamode microstructures embedded in water. Section 3 first establishes a unified inverse-design strategy containing all wave feature parameters of PMs. Then, four inverse-design categories, targeting four different types of PMs with properties on demand, are respectively formulated. Their topological and pentamode features are then compared in Section 4, followed by discussions on the formation mechanism of the broadband single-mode nature for the inverse-designed metamaterials. Subsequently, representative and simplified pentamode configurations with dominant geometrical features are proposed in Section 5. Finally, a dedicated pentamode metasurface device is designed in Section 6 for realizing prescribed wavefront manipulation within a broad subwavelength range for noise shielding. Section 7 highlights the main contributions of the study and gives the outlook of PM engineering.

2. Characterization of pentamode metamaterials

The PM to be considered in this work is a kind of specific periodic porous structure, which is supposed to be equivalent to a homogeneous medium whose wave behavior is similar to water. The so-called equivalence includes effective elastic modulus and mass density based on the effective medium theory (or homogenization theory). Hence, its wave motion can be characterized by the typical wave equation of a periodic porous microstructure. In a 2D PM, the in-plane time-harmonic wave propagation is governed by

$$(\lambda+2\mu)\nabla(\nabla\cdot\mathbf{u})-\mu\nabla\times(\nabla\times\mathbf{u})+\rho\omega^2\mathbf{u}=0, \tag{1}$$

where **u** denotes the displacement vector; λ, μ and ρ respectively represent the Lamé constants and mass density of the solid material; ω is the angular frequency; and ∇ is the Laplacian differential operator. Applying the Bloch periodic boundary conditions on the boundary nodes of the unitcell, classical eigenvalue problem under the plane strain assumption can be formulated and solved. Then, the final dispersion relations (**k**-ω) can be obtained after sweeping the Bloch wave vector **k** along the corresponding edges of the irreducible Brillouin zone.

Under the long-wavelength assumption, the effective medium approach can be adopted where the microstructure is regarded as equivalent to a dynamic effective medium. For elastic waves propagating in a periodic porous structure, the effective medium can be characterized by an elasticity tensor $\mathbf{C}^{eff}$ as:

$$\mathbf{C}^{eff} = \begin{bmatrix} K_x^{eff} & K_{xy}^{eff} & 0 \\ K_{xy}^{eff} & K_y^{eff} & 0 \\ 0 & 0 & G_{xy}^{eff} \end{bmatrix}, \tag{2}$$

where K_x^{eff} and K_y^{eff} are the effective elastic longitudinal moduli along the principal x- and y-directions, respectively; K_{xy}^{eff} denotes the effective coupling modulus along these two principle directions; and G_{xy}^{eff} signifies the effective shear modulus. Although several dynamic effective homogenization methods were employed in the field of elastic metamaterials (Lai et al., 2011; Liu et al., 2011a, 2011b; Dong et al., 2017), it is more effective, robust and universal to retrieve the effective elastic tensor by utilizing the dispersion relations within the long-wavelength limit (Martin et al., 2012; Chen et al., 2015; Cai et al., 2016), especially for very complex topologies. In this case, one can substitute the effective elasticity tensor in Eq. (2) into the Christoffel's equation for an anisotropic elastic medium (Achenbach et al., 2012) and then obtain the actual phase velocities along different propagation directions by

$$\begin{aligned} c_{\mathrm{L}x} &= \sqrt{K_x^{eff}/\rho^{eff}},\ c_{\mathrm{T}x} = \sqrt{G_{xy}^{eff}/\rho^{eff}}, \\ c_{\mathrm{L}y} &= \sqrt{K_y^{eff}/\rho^{eff}}, c_{\mathrm{T}y} = \sqrt{G_{xy}^{eff}/\rho^{eff}}, \\ c_{\mathrm{L}45} &= \frac{1}{4\rho^{eff}}\left[K_x^{eff} + K_y^{eff} + 2G_{xy}^{eff} + \sqrt{\left(K_x^{eff} - K_y^{eff}\right)^2 + 4\left(K_{xy}^{eff} + G_{xy}^{eff}\right)^2}\right], \\ c_{\mathrm{T}45} &= \frac{1}{4\rho^{eff}}\left[K_x^{eff} + K_y^{eff} + 2G_{xy}^{eff} - \sqrt{\left(K_x^{eff} - K_y^{eff}\right)^2 + 4\left(K_{xy}^{eff} + G_{xy}^{eff}\right)^2}\right], \end{aligned} \tag{3}$$

where $c_{\mathrm{L}x}$ ($c_{\mathrm{T}x}$) and $c_{\mathrm{L}y}$ ($c_{\mathrm{T}y}$) are the longitudinal (transverse) wave velocities along the principal x- and y-directions, respectively; $c_{\mathrm{L}45}$ ($c_{\mathrm{T}45}$) indicates the longitudinal (transverse) polarization velocity in the 45-degree direction; and ρ^{eff} is the effective mass density of the PM microstructure. Combing the above elasticity tensor and phase velocities, the equivalence between the phase velocity of the effective medium and that of the microstructure will induce the effective elastic moduli and effective impedance of the microstructure as

$$\begin{cases} K_x^{eff} = \rho^{eff} c_{\mathrm{L}x}^2,\ G_{xy}^{eff} = \rho^{eff} c_{\mathrm{T}x}^2, \\ K_y^{eff} = \rho^{eff} c_{\mathrm{L}y}^2,\ G_{xy}^{eff} = \rho^{eff} c_{\mathrm{T}y}^2, \\ K_{xy}^{eff} = \rho^{eff}\left[\sqrt{\left(c_{\mathrm{L}45}^2 - c_{\mathrm{T}45}^2\right)^2 - \left(c_{\mathrm{L}x}^2 - c_{\mathrm{L}y}^2\right)^2/4} - c_{\mathrm{T}x}^2\right], \\ Z_x^{eff} = \rho^{eff} c_{\mathrm{L}x}. \end{cases} \tag{4}$$

Eq. (4) shows that the longitudinal and shear moduli are respectively determined by the longitudinal and transverse wave velocities along the principle directions, and the coupling modulus is determined by the longitudinal and transverse wave velocities along the principal directions and the 45-degree direction. Note that K_{xy}^{eff} can either be positive or negative depending on the microstructures. A positive value means that the microstructure can support tensile or compressive stress state in both principle directions. Conversely, a negative one can only support the tension in one principal direction and the compression in the other. In view of the non-resonant nature and the long-wavelength limit, the effective mass density of the PM microstructure is directly defined by $\rho^{eff}=\rho_0\gamma_{\mathrm{s}}$, where ρ_0 is the mass density of the solid; and γ_{s} represents the solid occupancy rate within a unitcell. For both isotropic and anisotropic PM microstructures, the so-called pentamode feature has to satisfy $\alpha = |K_{xy}^{eff}|/\sqrt{K_x^{eff}K_y^{eff}} \approx 1$ and $\beta = G_{xy}^{eff}/\sqrt{K_x^{eff}K_y^{eff}} \approx 0$ simultaneously (Chen et al., 2015).

To characterize the steady-state dynamic response of PMs surrounded by background water, the corresponding equation of motion considering the fluid-solid coupling under a time-harmonic excitation writes (Gao et al., 2010)

$$\begin{bmatrix} \mathbf{K}_{\mathrm{s}} & \mathbf{S}_{\mathrm{fs}}^{\mathrm{T}} \\ 0 & \mathbf{K}_{\mathrm{f}} \end{bmatrix} \begin{Bmatrix} \mathbf{u} \\ p \end{Bmatrix} + i\omega \begin{bmatrix} \mathbf{C}_{\mathrm{s}} & 0 \\ 0 & \mathbf{C}_{\mathrm{f}} \end{bmatrix} - \omega^2 \begin{bmatrix} \mathbf{M}_{\mathrm{s}} & 0 \\ -\mathbf{S}_{\mathrm{fs}} & \mathbf{M}_{\mathrm{f}} \end{bmatrix} \begin{Bmatrix} \mathbf{u} \\ p \end{Bmatrix} = \begin{Bmatrix} 0 \\ P_{\mathrm{f}} \end{Bmatrix}, \tag{5}$$

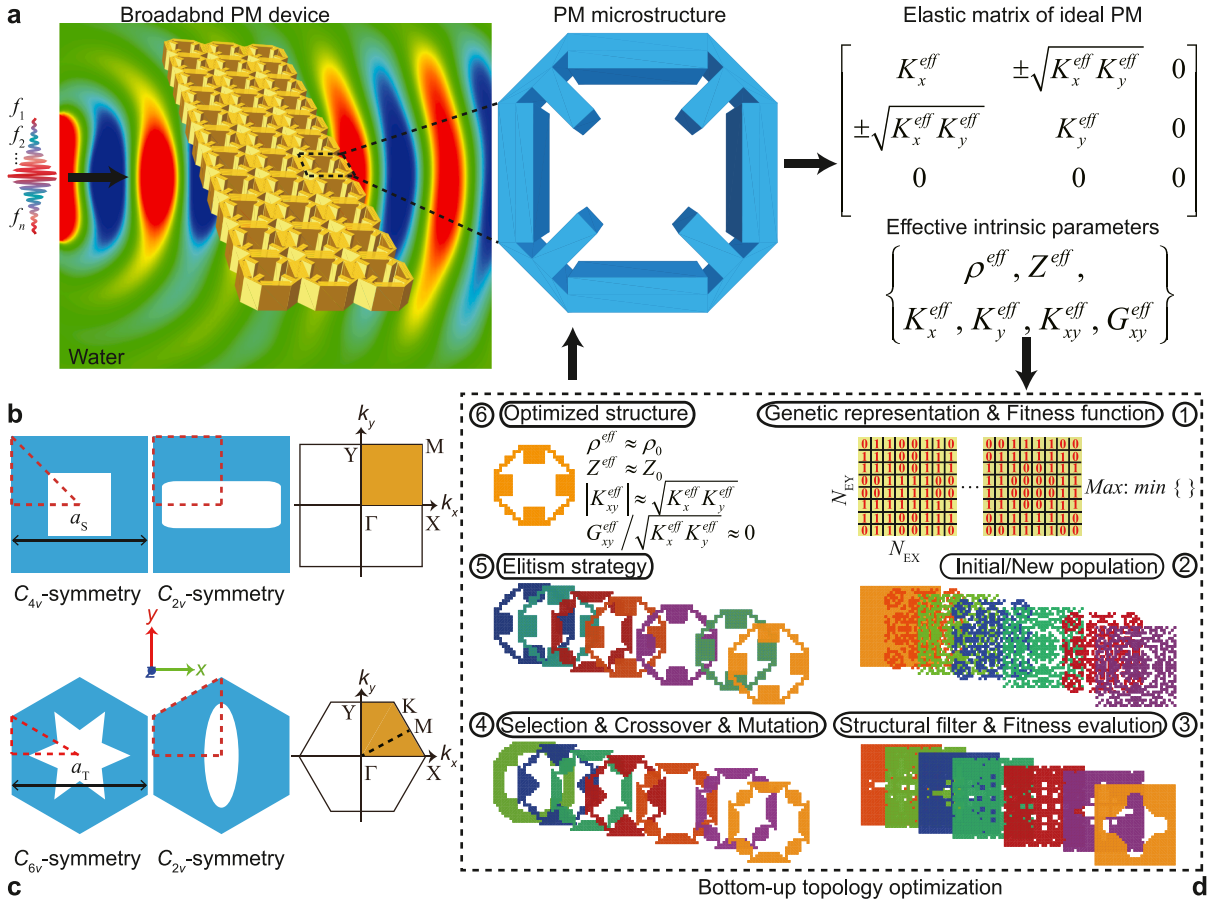

Fig. 1. Schematic of customized broadband pentamode metamaterials designed by bottom-up topology optimization. (a) Illustration of a broadband PM device for underwater wave manipulation. Broadband incident waves contain multiple operating frequencies from f_1 to f_n. The PM device consists of a series of representative C_{4v}-symmetry PM microstructures in a square lattice. **(b-c)** Representative design domains with prescribed structural symmetries (C_{2v}-symmetry, C_{4v}-symmetry, C_{6v}-symmetry) and the first Brillouin zone with irreducible parts shaded in brown of the microstructure in both square and triangle lattices. The red dash lines show the reduced design domains in optimization. **(d)** Procedure of the bottom-up topology optimization for designing a customized broadband PM microstructure. With genetic representation of binary matrices and suitably defined fitness function, the heuristic optimization generates the optimized PM microstructure on demand after sufficient rounds of evolution.

where $\mathbf{K}_s$ ($\mathbf{K}_f$), $\mathbf{C}_s$ ($\mathbf{C}_f$) and $\mathbf{M}_s$ ($\mathbf{M}_f$) are the stiffness, damping and mass matrices of the solid (fluid) parts, respectively; $\mathbf{S}_{fs}^T$is the transpose of the fluid-solid coupling matrix $\mathbf{S}_{fs}$; $\mathbf{u}$ and p respectively denote the displacement vector and the acoustic pressure of the finite element nodes; and P_f is the acoustic pressure applied on the fluid boundaries.

Considering water as an ideal compressible fluid in a lossless system, Eq. (5) can be simplified as

$$\begin{bmatrix} \mathbf{K}_s & \mathbf{S}_{fs}^T \\ 0 & \mathbf{K}_f \end{bmatrix} \begin{Bmatrix} \mathbf{u} \\ p \end{Bmatrix} - \omega^2 \begin{bmatrix} \mathbf{M}_s & 0 \\ -\mathbf{S}_{fs} & \mathbf{M}_f \end{bmatrix} \begin{Bmatrix} \mathbf{u} \\ p \end{Bmatrix} = \begin{Bmatrix} 0 \\ P_f \end{Bmatrix}. \tag{6}$$

By adopting the above in-plane wave dispersion relations, effective phase velocities, effective mass density, effective elastic moduli and steady-state wave motion equations of the fluid-solid coupling model to characterize dynamic properties of an arbitrary PM are obtained.

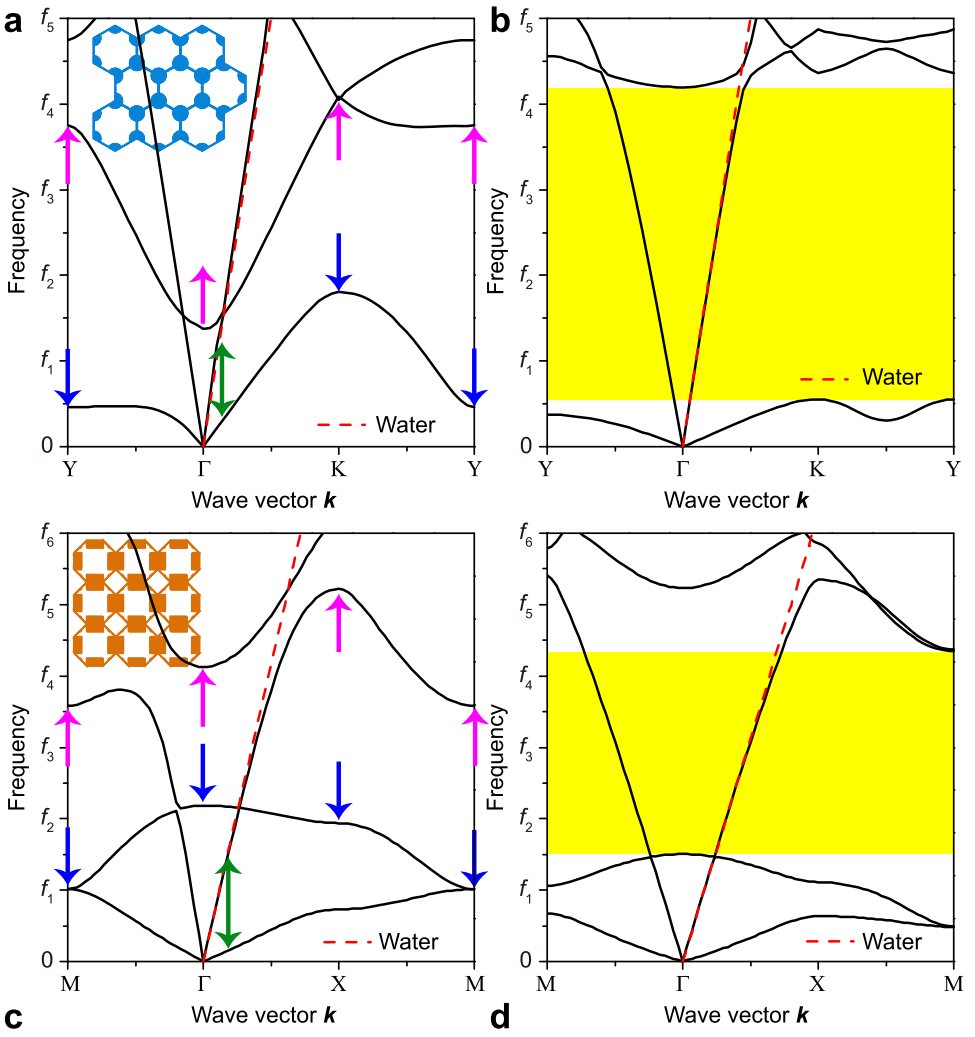

Fig. 2. Sketch of broadband single-mode design strategy by engineering dispersion relations. (a-b) Dispersion relations of a traditional honeycomb-lattice microstructure as shown in the inset (a) and an expected inverse-designed microstructure with the desired broadband single-mode range (b). **(c-d)** Dispersion relations of an analogical microstructure in square lattice as shown in the inset (c) and an expected inverse-designed broadband single-mode microstructure (d). The pink upward and blue downward arrows respectively represent the increasing and decreasing tendencies of a high-symmetric wave vector point. The green double-sided arrows indicate the expanding tendency between the transverse and longitudinal bands near Γ point. Red dash lines are the dispersion curves corresponding to water.

3. Inverse-design strategy for customized broadband pentamode metamaterials

Due to their water-like wave properties and solid nature, PMs show great potential for underwater acoustic applications. To rigorously realize a given underwater acoustic functionality, we set the target of constructing a broadband PM device shown in Fig. 1 (a) with customized mechanical properties, including macroscopic geometrical configuration, specific microcosmic $\mathbf{C}^{eff}$, ρ^{eff}, anisotropy and quasi-perfect impedance matching with water, all being prescribed *a priori*. For acoustic applications, water is always assumed to be compressible (Layman et al., 2013; Chen et al., 2017; Zhao et al., 2017; Sun et al., 2019) with, in most cases, negligible viscosity. The compressibility of a fluid medium provides elasticity which is the key to enable wave propagation. For metamaterials, the viscous effect on wave motion in water might be strong at high frequencies (Molerón et al., 2016), but rather weak at low frequencies, which can therefore be neglected (Cheng et al., 2015). Owing to the constant effective index of each PM microstructure, this PM device can give rise to the achromatic (frequency-independent and non-dispersive) property for the incident multi-wavelength waves. Obviously, the key is to systematically and tactically design the required microstructure with ρ^{eff} and the four arbitrary effective elastic moduli in Eq. (2). To build a unified and systematic inverse-design framework, we integrate all the effective moduli and the mass density into the construction of a specific and universal constraint including the pentamode feature, impedance matching degree and anisotropy of the PM. Meanwhile, the optimization model should avoid excessive narrow local minimal solid connection in order to guarantee the minimum mechanical strength of the entire microstructure.

The optimization model can inversely give rise to arbitrarily assigned effective parameter combination and even the extreme mass density and super-high anisotropy, as the backbone to achieve the customizable and almost perfect PM devices. The optimization problem can be solved by using any kind of existing optimization algorithms, such as the gradient-based optimization method (Bendsoe and Sigmund, 2013; Wang et al., 2003; Xie and Steven, 1993; Guo et al., 2014), non-gradient heuristic method (Holland 1975; Kirkpatrick et al., 1983) and even machine learning (Michie et al., 1994). Here, we select the genetic algorithm (GA) (Holland 1975; Dong et al., 2017, 2018, 2019, 2020). Considering the four representative symmetries of the microstructures in Fig. 1(b), only one-eighth, one-sixth or one-fourth of the microstructure is taken as the reduced design domain in the optimization. For any targeted broadband underwater acoustic device, both the macroscopic and microcosmic topologies need to be elaborately and simultaneously designed. The ultimately desired wave functionality governs the effective parameters of all microstructures which should support the ideal elastic matrix. Subsequently, the required effective intrinsic parameters of each microstructure can be deduced. These parameters become the design objective of the optimization model which can be converted into binary coding and decoding representations. Each involved microstructure is equivalent to an individual (chromosome) whose genes are decided by the pixels of the design domain. Since the tournament selection scheme is used here, the above proposed objective function is directly taken as the fitness function. The GA starts with an initial population including N_{p} binary $N \times N$ individuals. To speed up the convergence of the optimization, one individual is defined by a purely homogeneous solid microstructure without any void. In order to eliminate the checkerboard pattern, the "abuttal entropy filter" (Dong et al., 2017, 2018) is employed to improve the topology and the strength of the microstructures by removing some isolated pixels (finite elements) of 0 and filling up some isolated pixels of 1. According to the calculated eigenfrequencies, the fitness of each individual during the optimization is evaluated. Based on the fitness values and constraint satisfactions, all individuals are selected through the tournament selection scheme to breed a new generation (Dong et al., 2017, 2018, 2019, 2020). A set of genetic operations including the crossover and mutation are then applied to the current population for producing an offspring generation. Then the typical elitism strategy (Dong et al., 2017, 2018, 2019, 2020) is used at the end of each iteration by copying the best individual from the current generation into the next generation. After the prescribed generations (iterations), convergent solution leads to the optimized PM microstructure. Through assembling these optimized PM microstructures, a customized broadband achromatic acoustic PM device with high-efficiency is achieved.

The present optimization method is based on the homogenization theory and energy band (dispersion curve) theory. That is, the PM is seen to be equivalent to a homogeneous material which exhibits water-like properties and specific band structures. From the application point of view, the effective homogeneous material should exhibit orthotropic (incl. cubic and isotropic) elastic properties. This is the main reason why we select C_{2v} (orthotropic), C_{4v} (cubic) and C_{6v} (isotropic) symmetries, similar to many published papers on the homogenization of composite materials including metamaterials. In fact, if no symmetry is assumed for the microstructure, the traditional, low-order, linear homogenization theory can hardly describe the micro-behavior of the composite material. Note the application of high-order homogenization theory to metamaterial design is a long-lasting and challenging problem. As for the lattice form, square and triangle lattices are the most typical and commonly used micro-topology in the field of metamaterials. Particularly, almost all existing studies of pentamode metamaterials focus on triangle lattices.

In particular, C_{3v} symmetry is also a 120°-chiral symmetry for the triangle lattice. This symmetry may cause some special local boundary rotations especially for the microstructures with very few solid parts on the boundaries during optimization, which put the validation of the present low-order linear effective medium theory into jeopardy. Obviously, the lower symmetry will make this even more problematic. Therefore, we ignore the C_{3v} symmetry and only consider the representative symmetries of C_{2v}-, C_{4v}- and C_{6v} in the square and triangle lattices to provide the design principle for the customized broadband PMs.

In particular, a single-mode PM with exclusive longitudinal waves has been demonstrated for transformation-elastodynamic architectures (Martin et al., 2012). As shown in Fig. 2(a), traditional PMs are usually built upon honeycomb-lattice topology combined with symmetric solid blocks. Despite the ideal pentamode property, no single-mode range was found within the whole band structure. The interference of other multiple wave modes can significantly restrict or even jeopardize the potential acoustic functionalities, especially for devices based on transform acoustics. It should be pointed out that this multiple-mode character cannot be eliminated by only conducting the optimization of single pentamode feature parameters ($\alpha \approx 1$, $\beta \approx 0$) in Appendix A. Aiming at the lowest and widest possible single-mode frequency range, Fig. 2(a) and 2(b) show the necessity of minimizing the maximal value of the first band while maximizing the minimal value of the second band and the third eigenfrequency at Γ point simultaneously. Alternatively, as illustrated in Fig. 2(c) and 2(d), one can minimize the maximal value of the second band and the third eigenfrequency at Γ point while maximizing the minimal value of the third band and the fourth eigenfrequency at Γ point simultaneously. Consequently, the representative low- or high-order single-mode feature can be implemented within the broadband and low-frequency range. Meanwhile, the ideal pentamode nature can be faultlessly maintained. These two maximization schemes are referred to as the low- and high-order optimizations, respectively. To achieve the broadband single-mode property within the frequency range as low as possible, we suggest two ways to guide the inverse design of the microstructures under the premise of satisfying the pentamode feature: 1) expanding the frequency range between the first and second bands; or 2) expanding the second and third bands. Considering the four typical lattice symmetries in Fig. 1(b) and 1(c), the optimization of the PM microstructure can be holistically cast into the following formulation as

$$For: \ \Omega_{\mathrm{D}} = [\rho_1, \ \rho_2, \ \rho_3 \cdots \rho_i], \ (i = 1, \ 2, \cdots N \times N), \tag{7}$$

$$Maximize:\ O(\Omega_D)=\begin{cases} O_L=\dfrac{\left[\min\left(f_{2,\min},\ f_{3,\Gamma}\right)-f_{1,\max}\right]}{\left[\min\left(f_{2,\min},\ f_{3,\Gamma}\right)+f_{1,\max}\right]}, \\ O_H=\dfrac{\left[\min\left(f_{3,\min},\ f_{4,\Gamma}\right)-\max\left(f_{2,\max},\ f_{3,\Gamma}\right)\right]}{\left[\min\left(f_{3,\min},\ f_{4,\Gamma}\right)+\max\left(f_{2,\max},\ f_{3,\Gamma}\right)\right]}, \end{cases} \tag{8}$$

$$Subject\ to:\ \min_{\Omega_D}(\boldsymbol{w})\geq w_0, \tag{9}$$

$$\delta(\Omega_D)=max\left(\delta_{K_{xy}},\ \delta_{G_{xy}},\ \delta_{Z_x},\ \delta_\rho,\ \delta_{Ani}\right)\leq\delta_0, \tag{10}$$

where Ω_D represents the material distribution domain within the microstructural space, i.e., the design domain in Fig. 1(b) and 1(c), in which the solid and air materials are marked by 1 and 0, respectively; the whole design domain is divided into $N\times N$ finite elements (pixels); $\rho_i=0$ or 1 means the selected material of one pixel; O is the objective function; $f_{1,\max}$ ($f_{2,\max}$) is the maximal value of the first-order (second-order) eigenfrequencies at all high-symmetry wave vector points of the Brillouin zone; $f_{2,\min}$ ($f_{3,\min}$) is the minimal value of the second-order (third-order) eigenfrequencies at all high-symmetry wave vectors except Γ point (k_x=0, k_y=0) of the Brillouin zone; $f_{3,\Gamma}$ and $f_{4,\Gamma}$ are the third and fourth eigenfrequencies at Γ point; O_L (O_H) denotes relative single-mode range of the low- (high-) order band; $\boldsymbol{w}$ represents the arrays containing the sizes of all local air and solid components; w_0 is a prescribed minimal feature size parameter; δ is defined as the integral feature parameter of the microstructure; and δ_0 is a prescribed feature parameter which is expected to be a small value close to zero. The five feature parameters of δ are defined by

$$\delta_\rho=1-\frac{min(\rho^{eff},\ \rho_0\eta)}{max(\rho^{eff},\ \rho_0\eta)}, \tag{11}$$

$$\delta_{K_{xy}}=1-\frac{min\left(\left|K_{xy}^{eff}\right|,\ \sqrt{K_x^{eff}K_y^{eff}}\right)}{max\left(\left|K_{xy}^{eff}\right|,\ \sqrt{K_x^{eff}K_y^{eff}}\right)}, \tag{12}$$

$$\delta_{G_{xy}}=\frac{min\left(G_{xy}^{eff},\ \sqrt{K_x^{eff}K_y^{eff}}\right)}{max\left(G_{xy}^{eff},\ \sqrt{K_x^{eff}K_y^{eff}}\right)}, \tag{13}$$

$$\delta_{Z_x}=1-\frac{min\left(Z_x^{eff},\ Z_0\right)}{max\left(Z_x^{eff},\ Z_0\right)}, \tag{14}$$

$$\delta_{Ani}=1-\frac{min\left(K_y^{eff}\Big/K_x^{eff},\ \xi\right)}{max\left(K_y^{eff}\Big/K_x^{eff},\ \xi\right)}, \tag{15}$$

where δ_ρ, $\delta_{K_{xy}}$, $\delta_{G_{xy}}$, δ_{Z_x}, δ_{Ani} are the feature parameters of ρ^{eff},K_{xy}^{eff},G_{xy}^{eff},$Z_x^{eff}$and the anisotropy degree K_y^{eff}/K_x^{eff}, respectively; η is the prescribed normalized effective mass density; ξ is the prescribed anisotropy degree; and Z_0 denotes the acoustic impedance of water. In theory, a near-zero δ_ρ means that the microstructure can possess the expected mass density. Near-zero $\delta_{K_{xy}}$and $\delta_{G_{xy}}$ imply that the microstructure can effectively capture the ideal pentamode feature. Similarly, a near-zero δ_{Z_x}suggests that the microstructure can perfectly match with water. A near-zero δ_{Ani} indicates that the microstructure can support the expected anisotropy. Obviously, the constraint in Eq. (10) is crucial to ensure the microstructure which synchronously satisfies various customized features, to give rise to the best and microstructural possible topology.

In particular, the objective functions are classified by its low-order optimization (O_L) and high-order one (O_H) to scrutinize the effect of band features on the ultimate topological feature and pentamode feature. Note that, limited by the empirical nature of the designs, this effect has been ignored and could hardly be directly controlled when designing PMs in existing literature. In our case, however, the specific constraint in Eq. (10) can drive the evolution of the microstructure to end up with the optimal configuration with the best integral feature, i.e., gradually approaching typical pentamode character with $\alpha\approx1$ and $\beta\approx0$ while simultaneously approaching the desired mass density, impedance and even a customized anisotropy. Obviously, the multiple and rigorous physical and geometrical requirements make the present optimization problem in Eqs. (7)–(10) closer to the practical application but also poses tremendous challenges. As we known, an anisotropic PM with specific anisotropy is vital in transformation underwater acoustics. The optimization model in Eqs. (7)–(10) can generate the broadband single-mode PM while keeping the perfect impedance matching and a given anisotropic degree. In this sense, the inverse-designed microstructures can be called the anisotropic PMs with impedance matching and prescribed anisotropy degree.

Specific to different potential engineering applications and unwater acoustic functions, the optimization problem in Eqs. (7)–(10), designed as Category 1, can be further extended to the following three categories of PM optimization sub-models for generating the PM microstrcutures which support other types of wave motions.

(a) Category 2: Free isotropic PMs

One can perform optimization by only considering two pentamode feature parameters, namely $K_{xy}^{eff}$and G_{xy}^{eff}. In this case, only the optimization constraint in Eq. (10) needs to be adjusted and reduced to

$$\delta(\Omega_{\mathrm{D}}) = max\left(\delta_{K_{xy}},\ \delta_{G_{xy}},\ \delta_{\rho}\right) \le \delta_0, \tag{16}$$

where the objective function $O(\Omega_{\mathrm{D}})$ is replaced by the feature parameter δ of the microstructure. Clearly, the microstructure will be equivalent to an ideal metafluid when the two feature parameters are small enough. This optimization is a simple pentamode inverse-design problem, leading to microstructures which are called free PMs.

(b) Category 3: Isotropic/anisotropic PMs with impedance matching

In acoustic control, PMs are required to be perfectly matched with the background water. With the isotropic or anisotropic properties, the broadband single-mode PMs offer attractive features for underwater acoustics. The optimization constraint in Eq. (10) can then be replaced by

$$\delta(\Omega_{\mathrm{D}}) = max\left(\delta_{K_{xy}},\ \delta_{G_{xy}},\ \delta_{Z_x},\ \delta_{\rho}\right) \le \delta_0, \tag{17}$$

where the objective function for the single-mode range is still decided by O_{L} or O_{H}; and the anisotropy feature parameter δ_{Ani} of the specific feature constraint in Eq. (10) is removed, which is beneficial for the optimization to explore the widest single-mode range. In this case, the inverse-designed isotropic or anisotropic microstructures are called isotropic or anisotropic PMs with impedance matching, respectively.

(c) Category 4: Anisotropic PMs with prescribed anisotropy

When several layers of PM microstructures are assembled into an underwater acoustic cloak, only the outer-layer microstructures need to match with the background water. Therefore, for the interlayers, designing the highly anisotropic single-mode PM microstructures can not only improve the cloaking performance but also significantly decrease the number of the layers of the microstructures. Therefore, the optimization constraint in Eq. (10) rewrites

$$\delta(\Omega_{\mathrm{D}}) = max\left(\delta_{K_{xy}},\ \delta_{G_{xy}},\ \delta_{\rho},\ \delta_{Ani}\right) \le \delta_0, \tag{18}$$

where the impedance matching parameter of the specific constraint in Eq. (10) is removed. The inverse-designed microstructures are called the anisotropic PMs with prescribed anisotropy.

4. Optimization results of PMs and discussions

This section presents the optimization results with the prescribed combinations of effective intrinsic parameters using the low- and high-order topology optimization for wave motions. Representative topological features and pentamode features of some typical optimized microstructures are analyzed and discussed for both square and triangle lattices.

In all topology optimizations, the “coarse to fine” strategy (Dong et al., 2017) is adopted to obtain the fine-meshed microstructures while keeping reasonable computational cost. For square and triangle lattices, the lattice constant a is asset to be 0.03 m and 0.02 m, respectively. The square-lattice microstructure is composed of 60 × 60 pixels. The dimension of each pixel is $(a/60) \times (a/60)$. Similarly, a triangle-lattice microstructure contains rectangle elements with a dimension of$(a/60) \times (\sqrt{3}a/180)$. Unless explicitly stated, the minimal feature size parameter w_0 is set as $a/60$ for both the square and triangle lattices. Two materials, aluminum and lead, are used for the solids in the optimization, i.e., ρ_{Al}=2700 kg/m^3, E_{Al}=0.69 GPa, υ_{Al}=0.33; and ρ_{LE}=11,400 kg/m^3, E_{LE}=23.7 GPa, υ_{LE}=0.4066. The material parameters of water are: ρ_0 = 1000 kg/m^3, K_0=2.25 GPa, and Z_0=1.5 MPa.s/m. Genetic parameters used in GA are the population size N_{p}=30, crossover possibility P_{c}=0.9, mutate possibility P_{m}=0.03 and tournament competition group N_{ts}=21. Each topology-optimized microstructure is generated from six optimization runs with the same set of algorithm parameters. The generation numbers at the coarse and fine stages take 1000 and 2000, respectively. For the eigenfrequency calculation, four small wave vectors (low frequencies) are used to obtain the quasi-static effective moduli for both the isotropic and anisotropic microstructures. We select (k_x=0, k_y=0), (k_x=π/20a, k_y=0), (k_x=0, k_y=π/20a) and (k_x=π/20a, k_y=π/20a) for the x-direction, y-direction and 45-degree direction in the square-lattice case. In the triangle-lattice, we utilize four similar small wave vectors (k_x=0, k_y=0), (k_x=π/15a, k_y=0), (k_x=0, k_y=π/15a) and (k_x=π/15a, k_y=π/15a) for the three primary directions of interest. All optimizations are conducted on a Linux cluster with Intel Xeon Platinum 8168 @ 2.70 GHz. The complete inverse-design procedure to get a topology-optimized microstructure takes about 26.7 h. The eigenfrequency calculation, mode analyses, dispersion relation computation and effective parameter retrieval are accomplished by the commercial finite element software ABAQUS 6.14–1. The underwater acoustic full-wave propagation of inverse-designed PM devices is simulated by the commercial finite element software COMSOL Multiphysics 5.3.

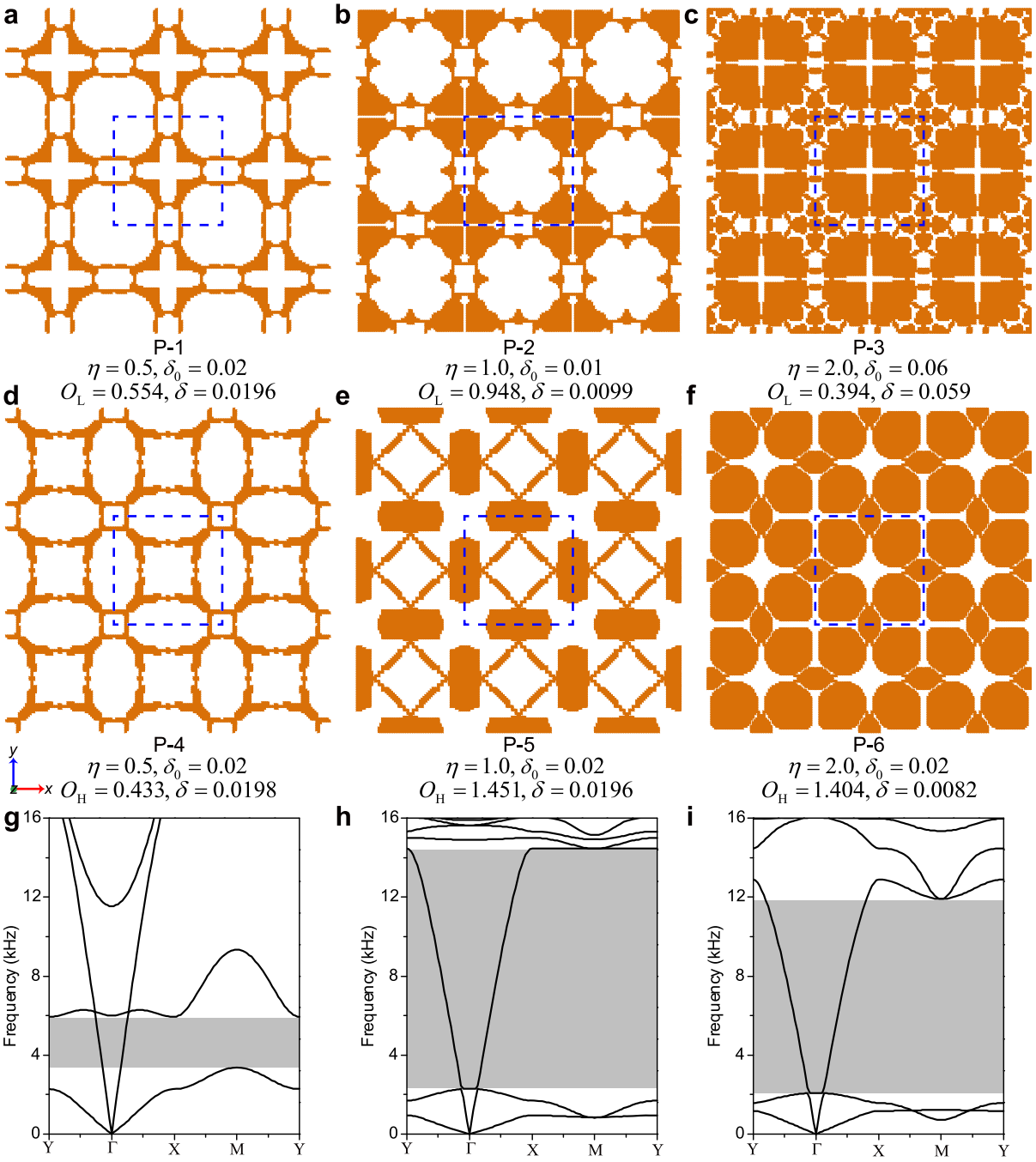

Fig. 3. Free isotropic square-lattice PMs. (a–c) Three 3 × 3 microstructures with their representative prescribed η and δ_0 using the low-order optimization. **(d–f)** Three 3 × 3 microstructures with their representative prescribed η and δ_0 using the high-order optimization. Dash line represents a C_{4v}-symmetry PM microstructure. **(g–i)** Dispersion relations from Bloch-wave analysis for P-1 (**g**), P-5 (**h**) and P-6 (**i**), respectively. The shadowed areas represent the bandgaps.

4.1. Free isotropic PMs

As defined in Eq. (16), the simplest strategy is to exclusively optimize two feature parameters, K_{xy} and G_{xy}, as detailed in Appendix A. However, the optimization model cannot induce single-mode feature. To create the broadband single-mode range and pentamode feature simultaneously, we employ the optimization model in Eq. (16) to create novel square-lattice and triangle-lattice high-symmetric PMs. As shown in Fig. 3, the topologically optimized microstructures from both low- and high-order optimizations share the common topological feature, i.e., several big solid blocks connected with small blocks by narrow connectors. All

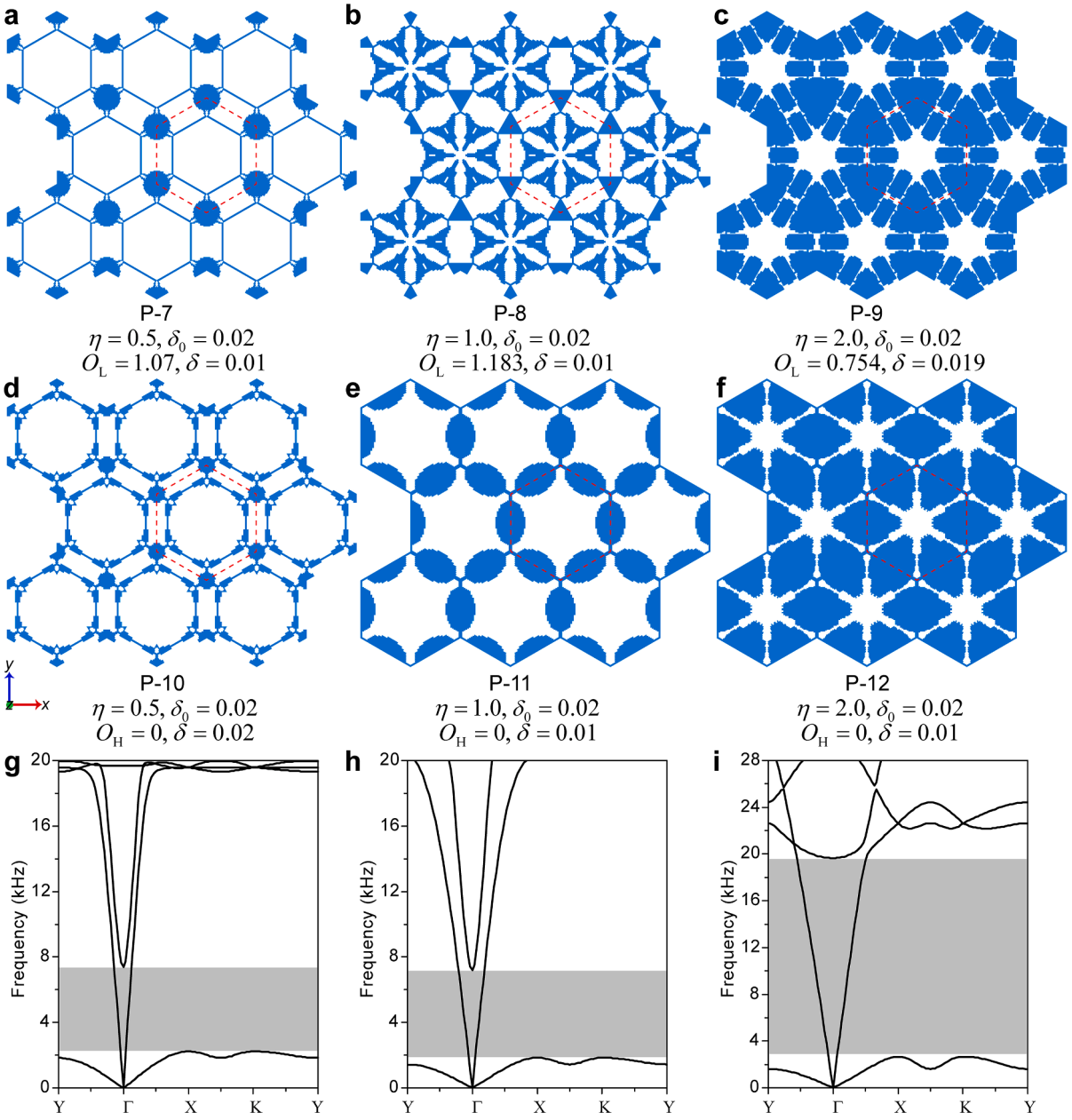

Fig. 4. Free isotropic triangle-lattice PMs. (a–c) Three 3 × 3 microstructures with their representative prescribed η and δ_0 using the low-order optimization. **(d–f)** Three 3 × 3 microstructures with their representative prescribed η and δ_0 for using the high-order optimization. Dash line represents a C_{6v}-symmetry PM microstructure. **(g–i)** Dispersion relations from Bloch-wave analysis for P-7 (**g**), P-8 (**h**) and P-12 (**i**), respectively.

microstructures, except P-3, offer good pentamode features and broadband single-mode ranges. Increasing the mass density, low-order microstructures in Fig. 3(a)–(c) embody more small blocks and larger big blocks. High-order microstructures in Fig. 3(d)–(f) mainly contain larger blocks. For small mass density (η=0.5), the low-order P-1 has larger relative bandwidth of single mode than the high-order P-4. For other η, however, the high-order microstructures show obvious superiority over the low-order ones. This indicates that the high-order optimization strategy is more suitable for free isotropic and single-mode PMs. As shown in Fig. 3(g)–(i), there are single longitudinal-mode bands within the complete bandgaps for other wave modes. In particular, the microstructures in Fig. 3(h) and (i) own very large relative band widths amounting to 145.1% and 140.4%, respectively. These new square-lattice topologies and expected broadband single-mode property demonstrate the effectiveness of our proposed optimization model.

Unlike the high-symmetry results in a square lattice, the higher-symmetry microstructures in the triangle lattice shows different features. We utilize the optimization model in Eq. (16) to further design new isotropic triangle-lattice microstructures in Fig. 4. Both the low- and high-order microstructures have the high-symmetric blocks attached to the latticed networks and narrow connectors. The

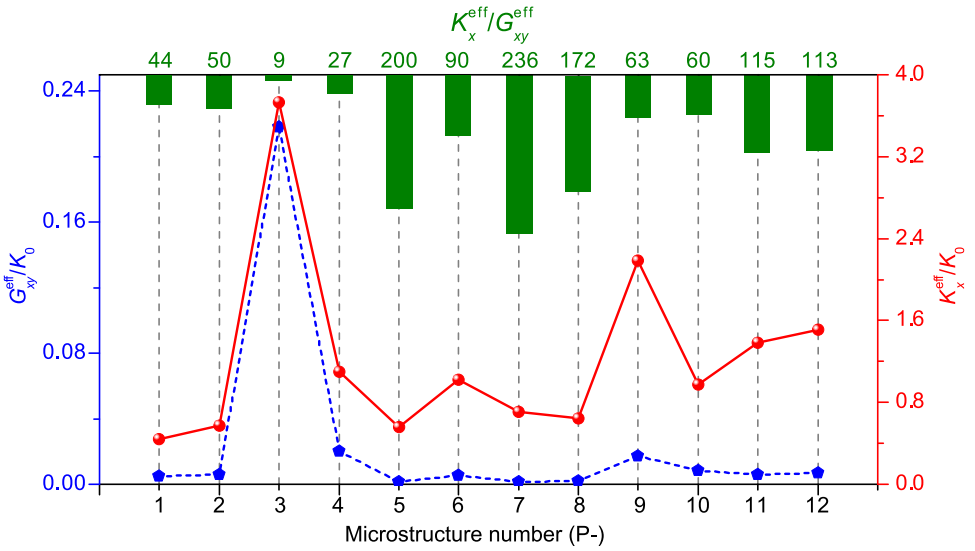

Fig. 5. Comparisons of the normalized effective parameters for free isotropic PMs. Performance of normalized shear and longitudinal moduli of PMs in Figs. 3 and 4 is illustrated. The green bars show the ratio of longitudinal modulus to shear modulus for the corresponding PM microstructure. Values of these ratio bars are also displayed.

high-order microstructures show different topological details from the low-order ones, including the number, location and geometry of the solid blocks. All microstructures show completely different topologies from the traditional honeycomb-lattice geometry (Layman et al., 2013; Hladky-Hennion et al., 2013; Zhao et al., 2017; Su et al., 2017; Chen et al., 2017; Sun et al., 2019). Microstructures P-7, P-8 and P-9 can enable broadband single-mode bandwidth with O_L=1.07, 1.183 and 0.754, respectively. However, Microstructures P-10, P-11 and P12 cannot produce any high-order single-mode range (O_H=0). Accordingly, for the present C_{6v}-symmetry triangle lattices, microstructures generated from the low-order optimization are more suitable to create broadband, low-frequency single-mode ranges of longitudinal waves. However, neither the low-order optimization nor high-order alone can realize high-order single-mode features. Fortunately, all microstructures in Fig. 4 can maintain ideal pentamode features with very small δ.

Comparing Fig. 3 with Fig. 4 shows that high-symmetric triangle-lattice PMs cannot behave like the high-symmetric square-lattice ones which can give rise to not only the low-order but also high-order single-mode ranges under neither the low-order nor the high-order optimization. Overall, a high-symmetric triangle-lattice system cannot produce the high-order single-mode range, but only bring about the low-order one. This is understandable since a higher symmetry implies a smaller searching space, thus making it more difficult for the topology optimization to achieve the required broadband single-mode property. For triangle lattices, multiple blocks with higher-symmetry ensure stronger resistance of the structure against bending, while resulting in rotational modes at high frequencies. However, high-order single-mode property requires low-frequency rotational modes. Therefore, these competing factors make it more difficult for the topology optimization to explore the broadband high-order single-mode range than the low-order one.

No matter whether the optimization is low-order or high-order, the free-from isotropic microstructures with C_{6v} symmetry in the triangle lattice are shown to be suitable to generate low-order single-mode features. Noted that the above observational conclusions are valid only for the present C_{6v}-symmetry triangle lattices. To draw a generalized conclusion, it is necessary to consider all kinds of the symmetries and lattices, which is a non-trivial task and goes beyond the scope of tis paper.

To scrutinize the dynamic differences between the microstructures in Fig. 4, Fig. 5 presents comparisons of the normalized effective longitudinal modulus and shear modulus. All microstructures, except P-3, have near-zero shear modulus. The effective longitudinal moduli of most microstructures are much larger than the shear moduli, showing the ideal pentamode feature. Different ratios of longitudinal modulus to shear modulus for all microstructures in Figs. 3 and 4 suggest that the triangle lattice outperforms the triangle lattice in terms of pentamode feature generation.

4.2. *Isotropic PMs with impedance matching*

To design the single-mode PMs with ideal impedance matching, we adopt the optimization model in Eq. (17) to explore the high-symmetric broadband PM microstructures under the specific low- and high-order optimizations for both square and triangle lattices. Fig. 3 presents the square-lattice microstructures with the prescribed normalized mass density η=0.5 (a, d), 1.0 (b, e) and 2.0 (c, f), respectively. Microstructures P-13, P-14 and P-15 are generated from the low-band optimization between the first and second bands. P-16, P-17 and P-18 are generated from the high-band optimization between the second and third bands. Clearly, these two kinds of optimization strategies lead to different topologies. In particular, both P-3 and P-6 show the lattice topological feature, suggesting that lattice-based geometry is a good choice for generating pentamode feature with a small mass density. For the low-band optimization

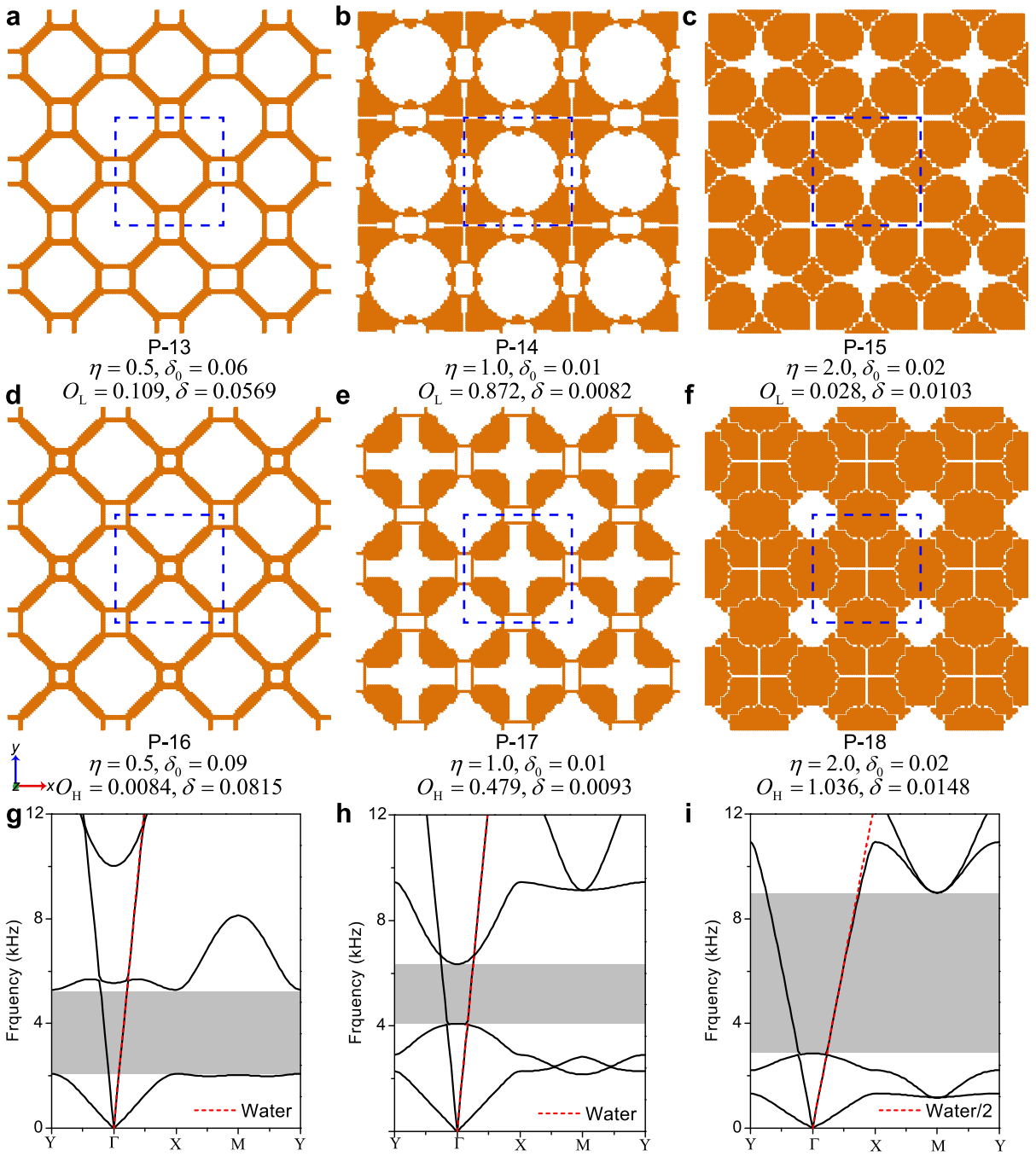

Fig. 6. Isotropic square-lattice PMs. (a-c) Three 3 × 3 microstructures with their representative prescribed η and δ_0 using the low-order optimization. **(d–f)** Three 3 × 3 microstructures with their representative prescribed η and δ_0 using the high-order optimization. Dash line represents a C_{4v}-symmetry PM microstructure. **(g–i)** Dispersion relations from Bloch-wave analysis for P-14 (**g**), P-17 (**h**) and P-18 (**i**), respectively.

results, solid blocks grow in size with prescribed η. Microstructure P-14 gives the best pentamode properties and the widest low-band single-mode range. Its network topology is composed of four big solid blocks, four small rods and several narrow connectors. Similarly, for the low-band optimization results, the solid blocks become bigger while the number of blocks increases as well. But Microstructure P-18 has the widest single-mode range with the relative bandwidth of 103.6%. In addition, the dispersion relations in Fig. 3(g) and 3(i) clearly demonstrate that P-14 and P-18 can effectively achieve the low-order and high-order broadband single modes, which are obviously superior to P-1 in Fig. 2. Comparing P-14 and P-17, the low-band optimized P-4 contains more solid blocks, which is beneficial for raising the frequency of the low-order rotational mode to realize the pentamode feature in the lower frequency regime.

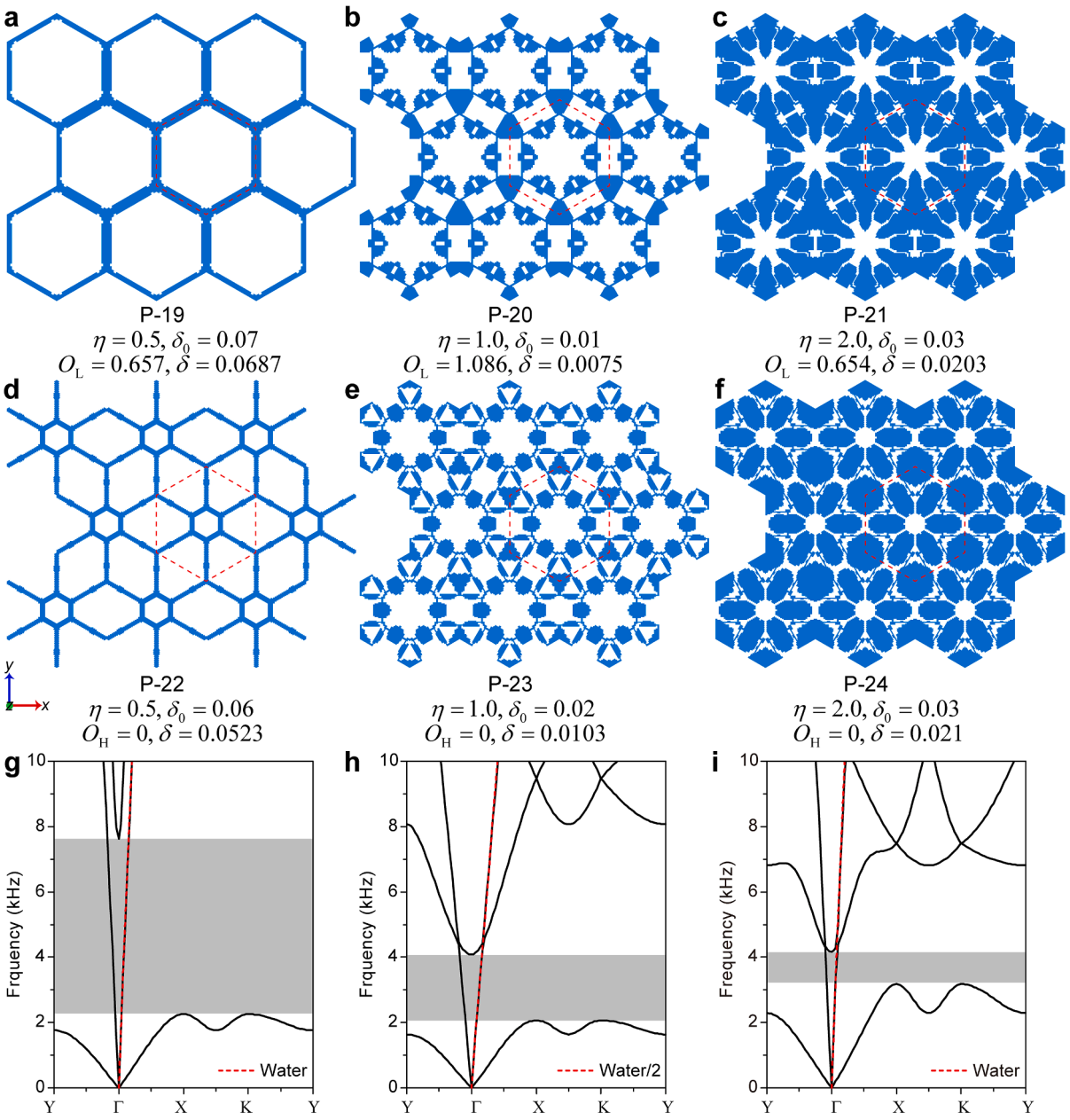

Fig. 7. Isotropic triangle-lattice PMs. (a-c) Three 3 × 3 microstructures with their representative prescribed η and δ_0 using the low-order optimization. **(d–f)** Three 3 × 3 microstructures with their representative prescribed η and δ_0 using the high-order optimization. Dash line represents a C_{6v}-symmetry PM microstructure. **(g–i)** Dispersion relations from Bloch-wave analysis for P-20 (**g**), P-21 (**h**) and P-23 (**i**), respectively.

Conversely, P-17 and P-18 can lower the low-order rotational mode and raise the high-order rotational mode, simultaneously.

To investigate the applicability of the optimization model in Eq. (17), Fig. 7 presents the C_{6v}-symmetry microstructures in triangle lattice. Interestingly, Microstructures P-19 and P-22 exhibit classical honeycomb-lattice topology for a given low mass density. This characteristic well demonstrates a new perspective in that the slenderness ratio is indeed beneficial for the pentamode feature. Of course, this indirectly verifies the correctness of our proposed optimization model. With an increasing η, solid blocks get bigger out of both low- and high-order optimizations. This also suggests that multiple symmetric big solid blocks allow raising the rotational modes, thereby realizing the broadband low-order single modes of longitudinal waves. Meanwhile, the commonly-used honeycomb configurations (Layman et al., 2013; Hladky-Hennion et al., 2013; Zhao et al., 2017; Su et al., 2017; Sun et al., 2019) can only offer low effective density, typically with η<1.0. When a large density (η>1.0) is required, slender rods in a honeycomb microstructure have to

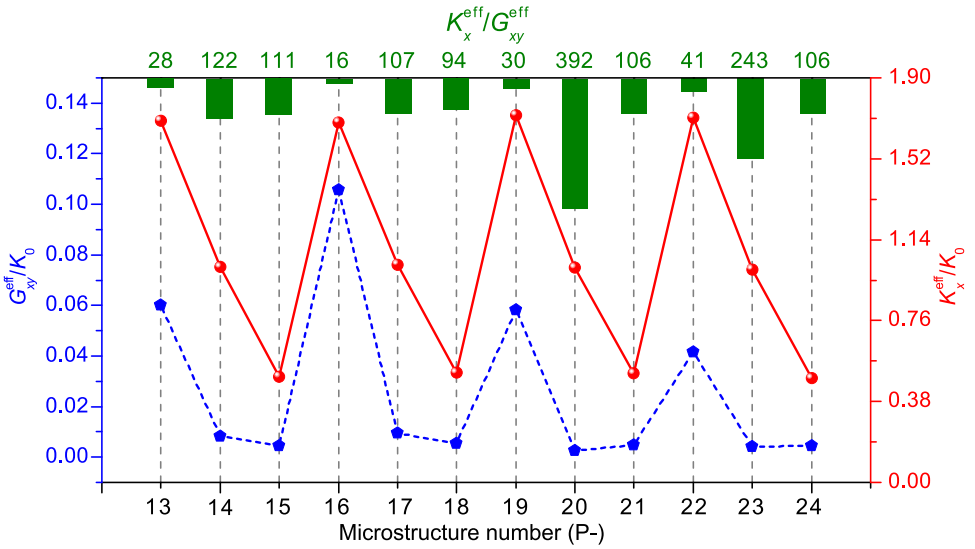

Fig. 8. Comparisons of the normalized effective parameters for isotropic PMs. Performance of the normalized shear and longitudinal moduli of PMs in Figs. 6 and 7 is illustrated. Green bars show the longitudinal-shear modulus ratio for the corresponding PM microstructures. Values of these ratio bars are also displayed.

become thicker, which in turn reduces the slenderness ratio of the microstructure. However, only a large enough slenderness ratio would provide the microstructure with the ideal pentamode feature. For various effective densities, the present inverse-design strategy can effectively create the required topology, thus breaking the limits of the commonly used traditional honeycomb configurations. The beneficial topology typically features multiple symmetric solid blocks with narrow connectors. Comparing the dispersion relations in Fig. 7(g)–(i), we notice that the microstructures with the low-order single mode are obviously superior to those with a high-order one. Microstructure P-23 also has a narrow low-order single-mode frequency range. Like the free-form isotropic triangle-lattice PMs in Section 4.1, for topology optimization of isotropic PMs with impedance matching, the C_{6v}-symmetry triangle-lattice topology is more likely to generate the broadband low-order single-mode pentamode feature, rather than the high-order one.

To further compare the isotropic microstructures with impedance matching in Figs. 6 and 7, Fig. 5 illustrates the normalized longitudinal modulus, shear modulus and the longitudinal-shear modulus ratio for all considered microstructure. All microstructures, except the ones with small density (P-13, P-16, P-19 and P-22), have very small shear modulus. Compared with the square lattice, the triangle-lattice Microstructures P-20, P-21, P-23 and P-24 possess smaller shear modulus. Since the impedance matching is considered in the optimization, the longitudinal modulus exhibits a linear variation with the increase of the imposed mass density. In particular, most microstructures with η=1.0 and η=2.0 have very large modulus ratios around 100. Moreover, the modulus ratio of P-20 can reach as high as 392, showing excellent pentamode feature. Overall, the triangle-lattice system is better than the square-lattice one for the isotropic PM property.

4.3. *Anisotropic PMs with impedance matching*

Using the optimization model in Eq. (17) with the lower symmetry assumption, we obtain the C_{2v}-symmetry anisotropic PM microstructures shown in Fig. 9. Compared with the microstructures in Fig. 6, the C_{2v}-symmetry ones are obviously more beneficial to expand the single-mode bandwidth, for either the low-order or high-order ranges. P-26 is very similar with P-14, which means that the high symmetry is good enough for the broadband single mode with η=1.0.

For both low- and high-order optimizations, solid blocks increase in both size and number. Comparisons with P-25, P-28 show similar four solid blocks in the middle range of the microstructure but two big blocks in the left and right sides. Compared with P-29, P-26, the present configuration involves more solid blocks and the lower anisotropy. Compared with the low-order case, P-28, P-29 and P-30 have larger single-mode frequency ranges. These observations imply that the topological features (in terms of size, number and distribution) of the solid blocks significantly dominate the formations of both broadband low- and high-order single-mode frequency ranges. Comparisons between the isotropic and anisotropic results in Figs. 6 and 9 suggest that the anisotropy can significantly improve the single-mode bandwidth. The anisotropy from the high-order optimization promotes the broadband and even ultra-broadband single modes of the longitudinal waves.

To further show the explicit effect of the topology on the broadband single-mode characters, we show the evolution histories of the low-order P-26 and high-order P-29 in Fig 10. It is observed from Fig. 10(a) (the 85th generation) and (c) (the 140th generation) that the inverse design can quickly capture the beneficial topological features in the early stages. With the evolution, the rotational mode mostly decreases with undulation in some generations. At the same time, both the shear and longitudinal modes decline as well, with

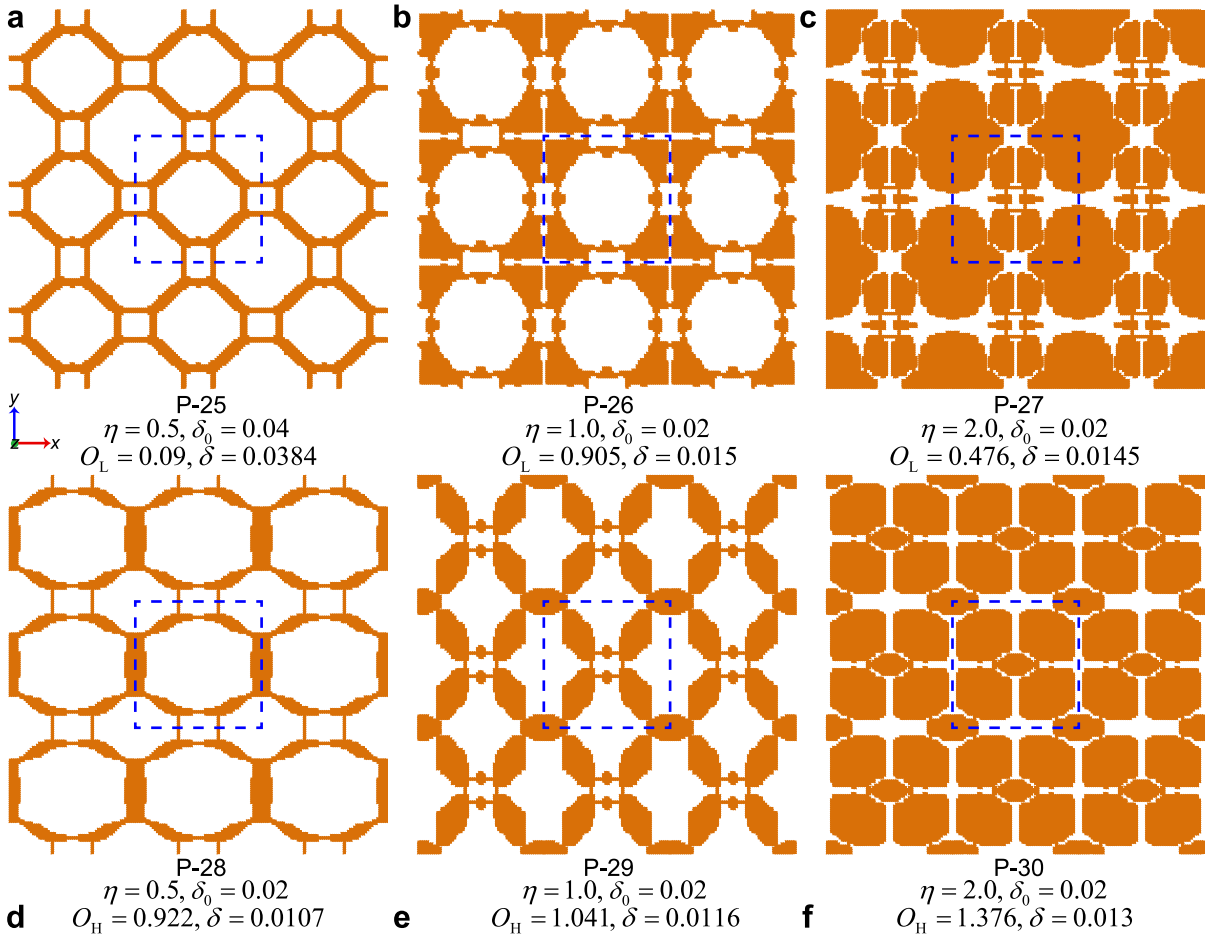

Fig. 9. Anisotropic square-lattice PMs. (a–c) Three 3 × 3 microstructures with their representative prescribed η and δ_0 using the low-order optimization. **(d-f)** Three 3 × 3 microstructures with their representative prescribed η and δ_0 using the high-order optimization. The dash line represents a C_{2v}-symmetry PM microstructure.

some fluctuations. In view of the similar evolutions of the shear and longitudinal modes in Fig. 10(b) and (d), the prominent distinction between the low- and high-order optimizations should be the reduction degree of the rotational mode from a homogeneous solid. Therefore, a stronger anisotropic extent yields a lower rotational mode. In another word, the resistance to bending of the microstructure can be adjusted by the solid blocks and anisotropy.

To check the effect of reduced triangle-lattice symmetry, we still utilize the optimization model in Eq. (17) to create several novel C_{2v}-symmetry microstructures as shown in Fig. 11. Overall, all anisotropic microstructures in Fig. 11 show significant superiority over the isotropic ones in Fig. 4 in terms of both single-mode bandwidth and integral pentamode feature parameter δ. Most anisotropic microstructures, expect P-34, show simpler topology than those in Fig. 7. The main topological difference between the isotropic and anisotropic microstructures is the distribution of big solid blocks. For Microstructures varying from η=1.0 to η=2.0, the number of solid blocks does not change, showing the robustness of the optimized topology. In short, for the present C_{2v}-symmetry triangle-lattice system, the geometry with ortho-symmetric and multiple solid blocks connected by the slender rods is a suitable topology to obtain broadband and even ultra-broadband (>150%) single-mode pentamode properties, while keeping the ideal impedance matching.

Note that it is extremely difficult to ascertain the underlying physics with the aid of analytical models. Instead, we try to qualitatively explain the reason behind. We would argue that the ortho-symmetric solid blocks can suppress the undesired coupling between the longitudinal and shear waves. In another word, the ortho-symmetric topology can easily change the resistance to bending of the slender rod. A weaker resistance to bending will result in lower rotational modes. As a result, a large mode bandgap would appear for the rotational-mode waves.

Similarly, the evolution histories of the low-order P-33 and high-order P-36 are depicted in Fig. 12 to show the effect of the structural topology. The evolution curves for the shear and longitudinal modes, show a very similar pattern. Shear and longitudinal modes can reach the ideal frequencies at the very early stage of generations. This demonstrates the effectiveness of the developed

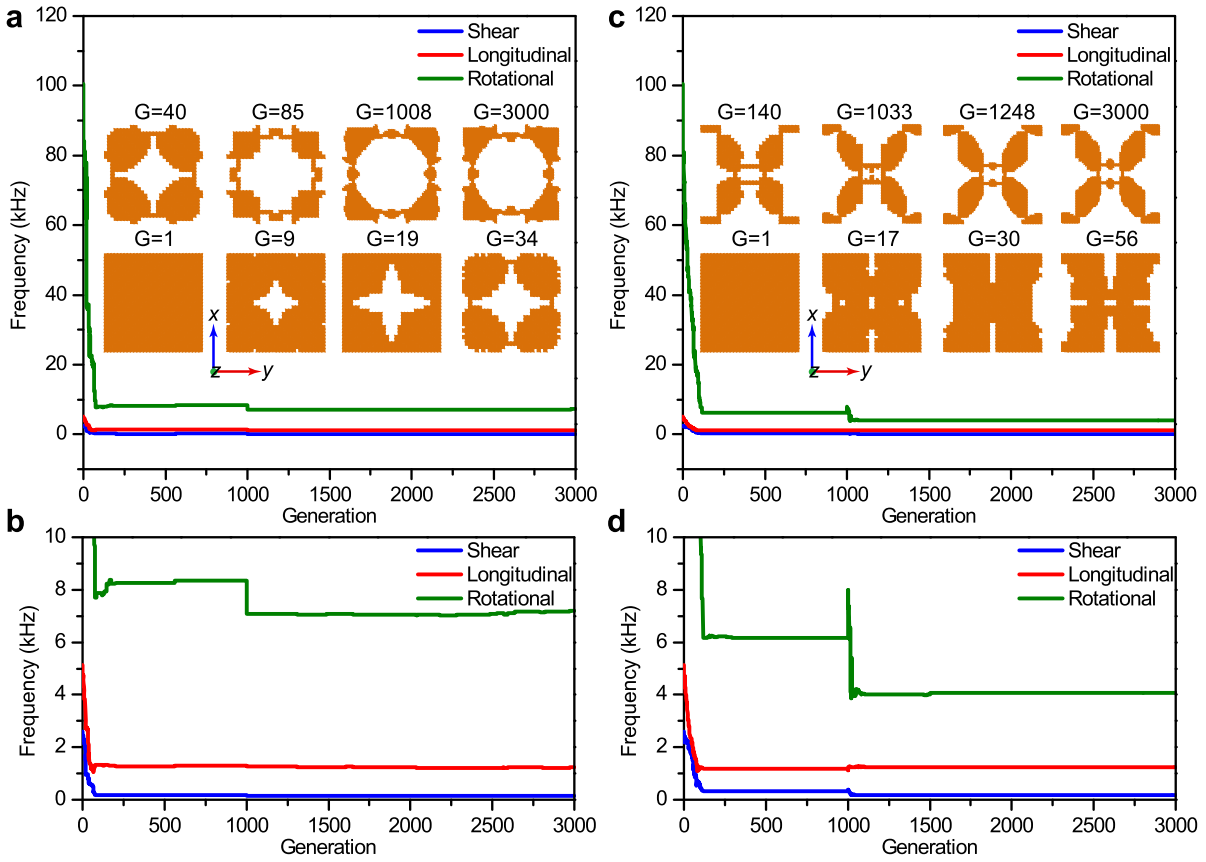

Fig. 10. Evolution histories of P-26 and P-29. (a, c) Evolution of the eigenstate frequencies of shear, longitudinal and rotational modes at $\boldsymbol{k}=(k_x=\pi/20a,\ k_y=0)$ for microstructures P-26 (a) and P-29 (c), respectively. **(b, d)** Enlarged evolution results of (a) and (b), respectively.

inverse-design model for PMs. Fig. 12(b) and (d) show drastic differences in the evolutions of P-33 and P-36. Microstructure P-33 can give rise to a very high rotational mode. Conversely, the rational mode of P-36 is very close to the longitudinal one. In fact, P-33 and P-36 share the similar local topological feature, i.e., the upper and lower parts are composed of four blocks attached to the slender rods. However, their left and right parts are different, i.e., one has two big blocks but the other one owns six blocks. Accordingly, the number and the distribution of blocks dominate the resistance to bending and then decide the location of the rotational mode.

In principle, it is impossible to scrupulously judge the upper bound on the number of solid blocks. But all inverse-designed PMs shown in Figs. 3, 4, 6, 7, 9 and 11 represent specific numbers of blocks for η=0.5, 1.0 and 2.0. Since the adopted material is aluminum whose relative density with respect to the water is η=2.7, we find it difficult to achieve a PM with η>2.0 based on many optimization testes. A larger effective density would require more blocks, as shown in Figs. 3, 4, 6, 7, 9 and 11. Therefore, our guess is that the microstructures with η=2.0 might represent the upper bound on numbers of blocks for all cases investigated in this paper. However, this should be understood in the proper context described in the paper.

To quantify the difference between the results in Figs. 9 and 11, Fig. 13 presents the normalized longitudinal modulus, shear modulus and of longitudinal to shear modulus ratio in Fig. 13(a) and the anisotropy degree K_y^{eff}/K_x^{eff} in Fig. 13(b) for each microstructure. Unlike Fig. 8, the longitudinal modulus of anisotropic microstructures displays complex and nonlinear variation with the increase of η. This implies that the anisotropy increases the complexity of the optimization because of larger search space. The anisotropic microstructures except P-25 and P-31 in Fig. 13, have very small shear modulus which is smaller than the isotropic ones in Fig. 8. P-27, P-28, P-32, P-34, P-35 and P-36 all possess very large modulus ratio. It is seen from the anisotropy degree in Fig. 13(b) that P-30 reaches the largest one followed by P-27. Other microstructures can only support the anisotropy degree smaller than 3.0. This means that the square-lattice C_{2v}-symmetry topology can induce higher anisotropy than the triangle-lattice C_{2v}-symmetry one does in addition to the ideal broadband single-mode pentamode feature.

4.4. Anisotropic PMs with prescribed anisotropy

Combing PMs with the transformation acoustics for underwater acoustic cloaking requires the outer-layer microstructures be matched with water. The stronger anisotropy of the other inner-layer microstructures means fewer layers of the cloak. Using the optimization model in Eq. (18), we inversely design three kinds of highly anisotropic microstructures for both square and triangle

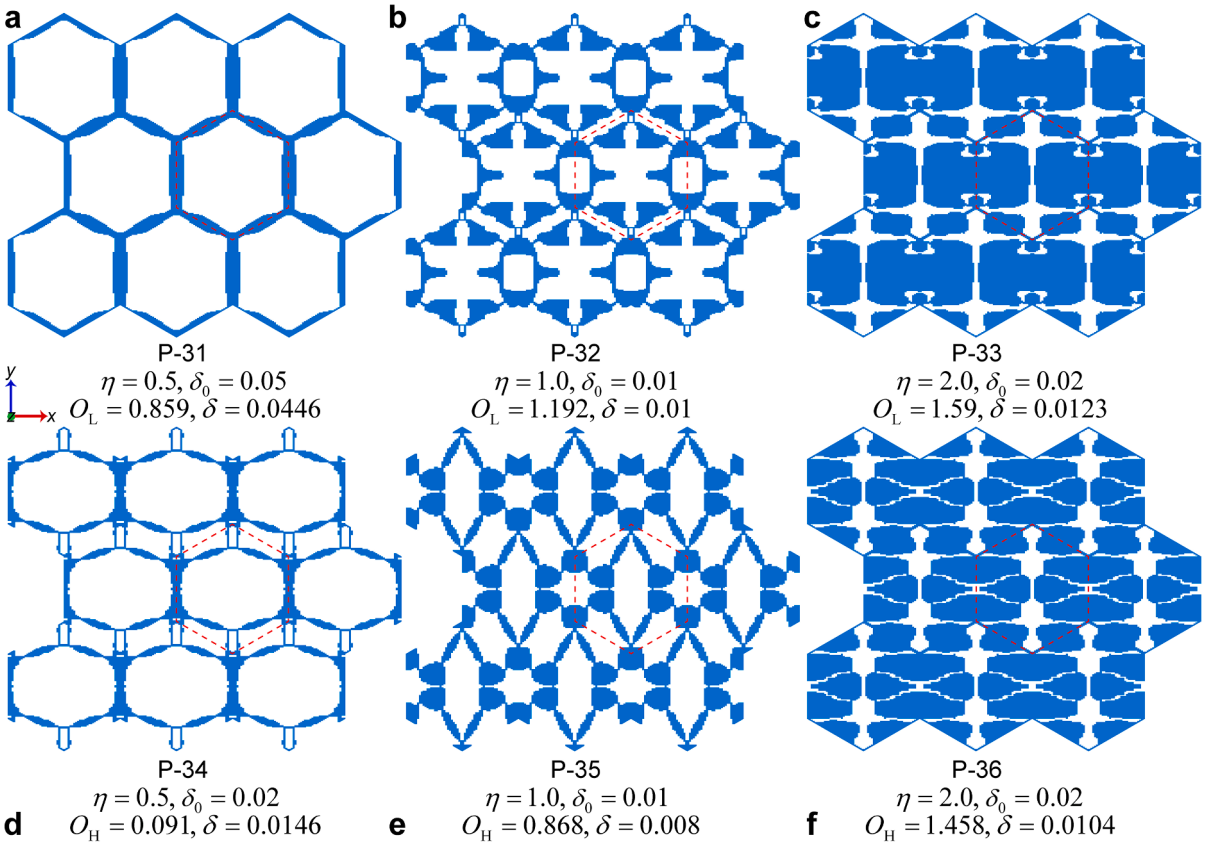

Fig. 11. Anisotropic triangle-lattice PMs. (a-c) Three 3 × 3 microstructures with their representative prescribed η and δ_0 using the low-order optimization. **(d–f)** Three 3 × 3 microstructures with their representative prescribed η and δ_0 using the high-order optimization. Dash line represents a C_{2v}-symmetry PM microstructure.

lattices as shown in Fig. 14(a)–(c). With the increasing anisotropy degree from 10 to 100, the low-order single-mode bandwidth increases for the square lattice. Three square-lattice anisotropic microstructures have the common topological features: four small solid blocks in the left and right edges, and two big blocks in the upper and lower edges connected by six slender rods. Interestingly, this specific geometrical feature suggests that it is very effective and easy to achieve highly anisotropic PMs with the different required anisotropy after adjusting the local parameters of the microstructures based on the topological features of P37, P-38 and P-39. Meanwhile, the single-mode range with a certain bandwidth also can be guaranteed.

Similarly, the same inverse-design strategy is used to design triangle-lattice microstructures with high anisotropy as shown in Fig. 14(d)–(f). Compared with the square-lattices in Fig. 14(a)–(c), the triangle-lattices can give rise to a larger single-mode range. However, it is worth noting that the exact feature parameters δ of the triangle-lattice microstructures are worse than those of the square-lattice ones. This demonstrates that the square-lattice is more suitable for constructing ultra-high anisotropy. But the triangle-lattice system shows obvious advantages in realizing the broadband single-mode feature. Three triangle-lattice microstructures also share similar topological features, i.e., four big solid blocks and two small blocks connected by four curved connectors. The essential difference among these three microstructures is the location and the size of the small blocks. That is, the small blocks locate on the left and right when the requested anisotropy is 10, while locating on up and down when the anisotropy increases to 100. Therefore, the anisotropic topological feature in Fig. 14(d)–(f) can be taken as a novel structural foundation to design PMs with arbitrary high anisotropy for better acoustic cloaking.

Unlike the present results from the low-order optimization, it is noted here that the high-order optimization cannot maintain the broadband single-mode frequency range and ultra-high anisotropy simultaneously. The resulting performances in Fig. 14 should represent the limit for this kind of highly anisotropic PMs.

To better show the anisotropy of the microstructures in Fig. 14, Fig. 15 illustrates the corresponding effective longitudinal and shear wave phase velocities with respect to the propagation direction. ΓX and ΓY correspond to the 0- and 90-degree directions, respectively. All anisotropic microstructures possess weak anisotropy for the shear phase velocity. But their longitudinal phase velocities show very high anisotropy. As the propagation direction changes from the ΓX to ΓY, the longitudinal phase velocity becomes larger and larger, before finally reaching the maximal value at the 90-degree direction. The longitudinal phase velocity ration between the 90- and 0-direction also verifies the correctness of the anisotropy degree observed in Fig. 15.

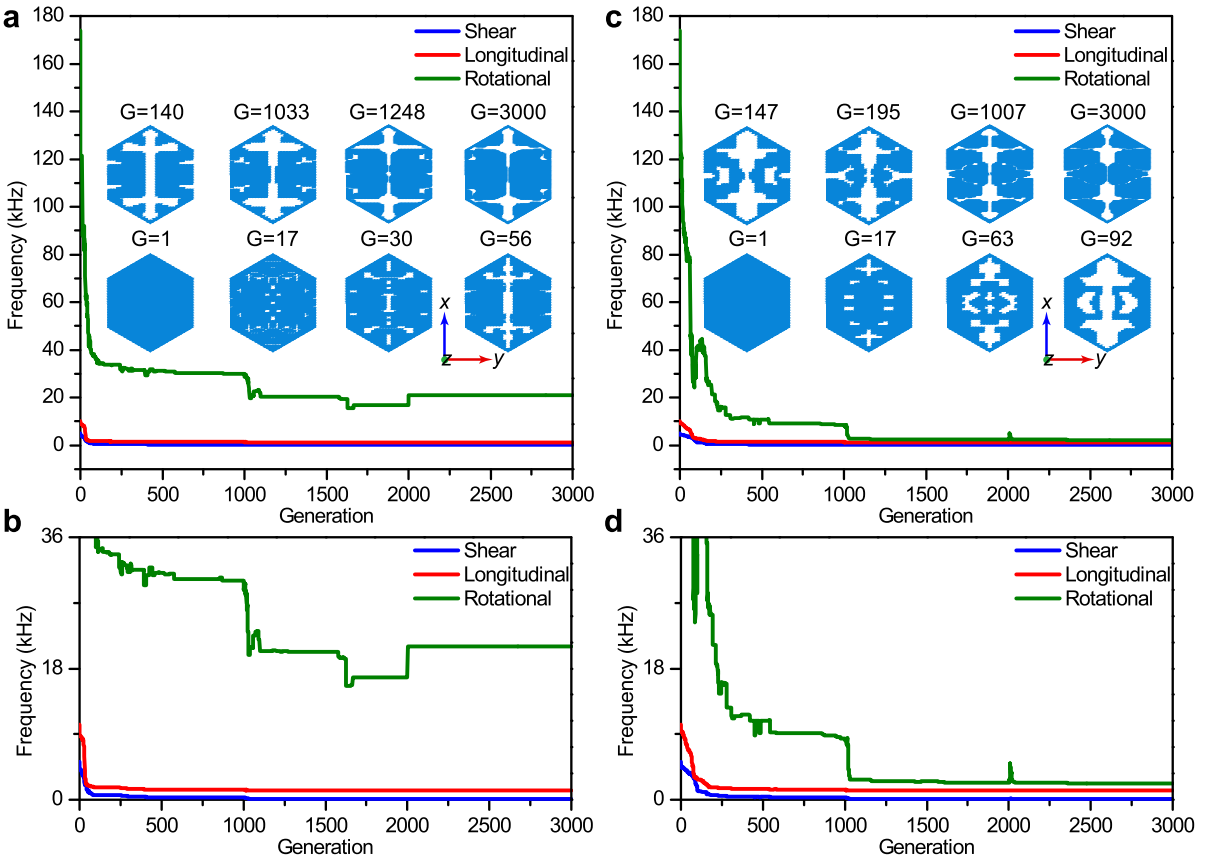

Fig. 12. Evolution histories of P-33 and P-36. (a, c) Evolution of the eigenstate frequencies of shear, longitudinal and rotational modes at $\boldsymbol{k}$=(k_x=π/15a, k_y=0) for the microstructures P-33 (a) and P-36 (c), respectively. **(b, d)** Enlarged evolution results of (a) and (b), respectively.

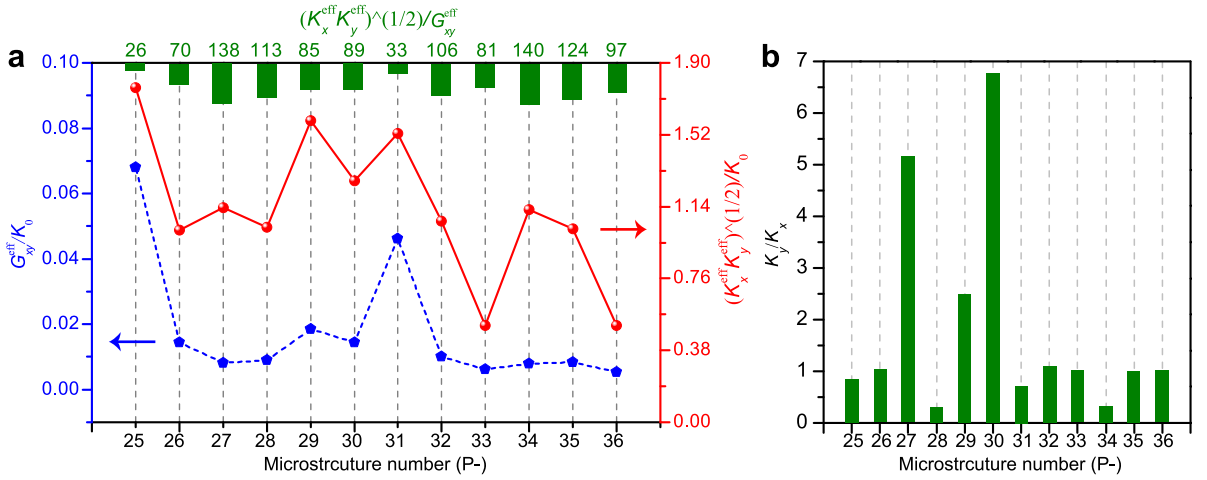

Fig. 13. Comparisons of the normalized effective parameters and feature parameters for anisotropic PMs. (a) Performance of normalized shear and longitudinal moduli of PMs in Figs. 9 and 11. Green bars show the ratio of longitudinal modulus to shear modulus for the corresponding PM microstructure. Values of these ratio bars are also displayed. **(b)** Anisotropy degreess of PMs in Figs. 9 and 11.

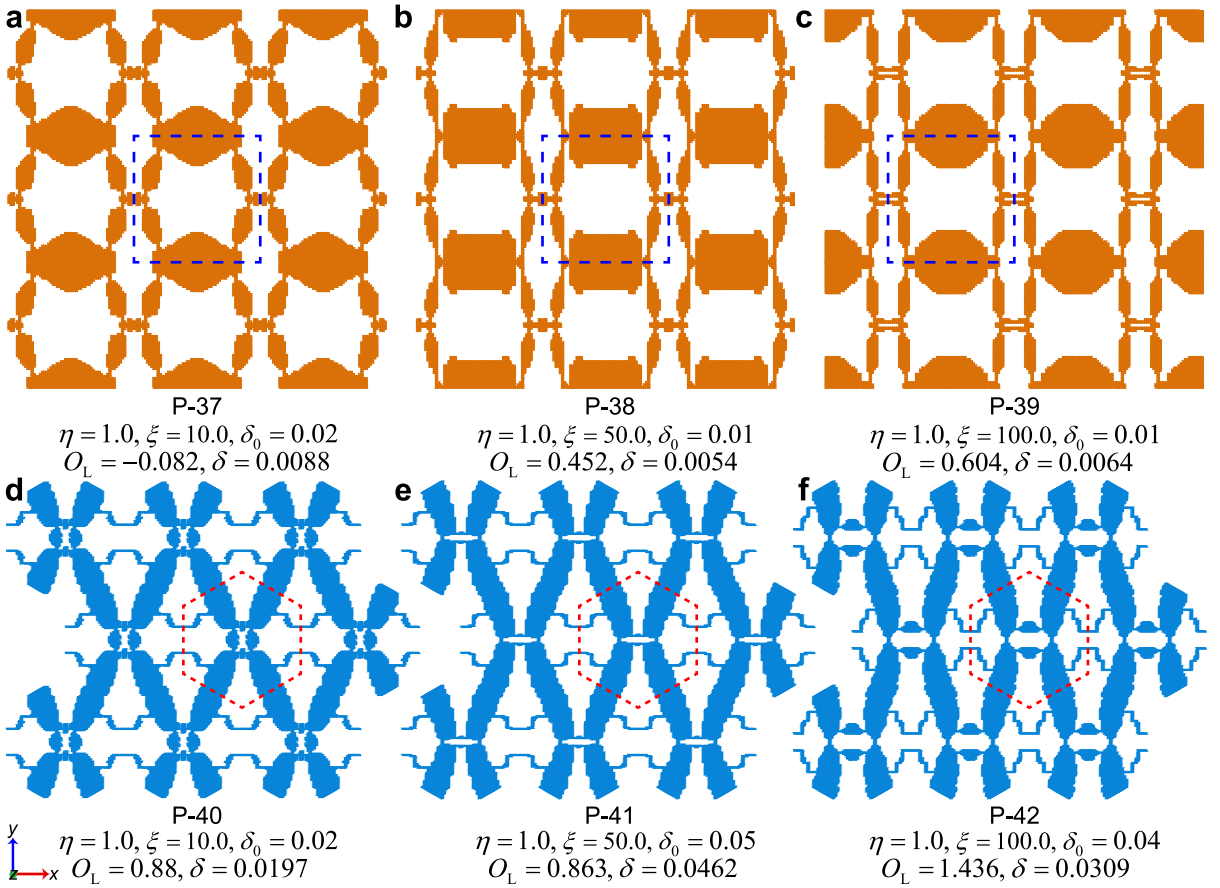

Fig. 14. Highly anisotropic PMs. (a-c) Three 3 × 3 microstructures with their prescribed anisotropic extents (ξ=10.0, 50.0, 100.0) in the square lattice using the low-order optimization. **(d–f)** Three 3 × 3 microstructures with their prescribed anisotropic extents (ξ=10.0, 50.0, 100.0) in the triangle lattice using the low-order optimization. Dash line represents a C_{2v}-symmetry PM microstructure.

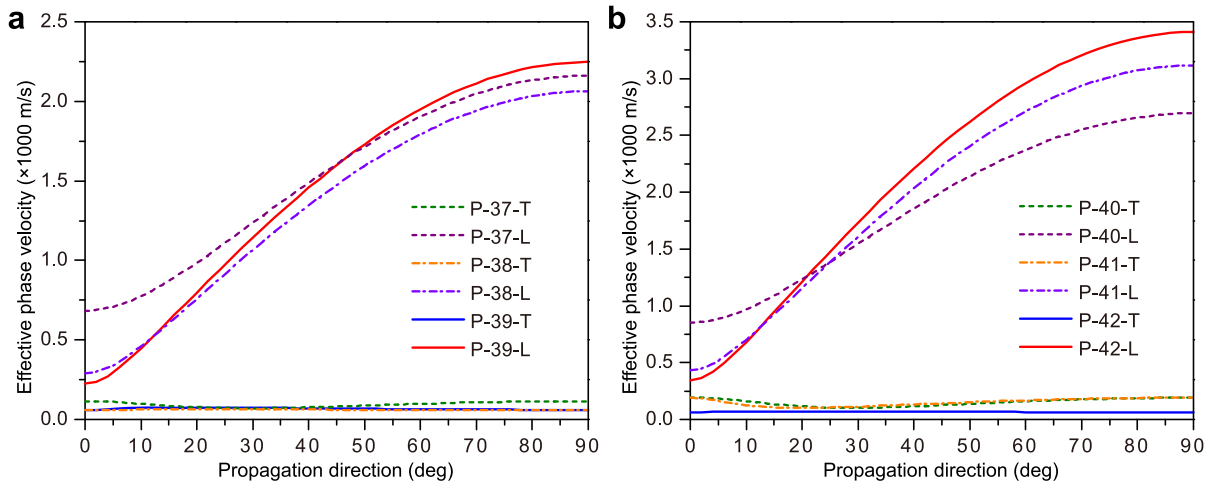

Fig. 15. High anisotropy of PMs in Fig. 14. Effective phase velocities of the square-lattice (a) and triangle-lattice (b) microstructures in Fig. 14 under different propagation directions varying from 0° (ΓX) to 90° (ΓY). T and L represent the shear and longitudinal wave modes, respectively.

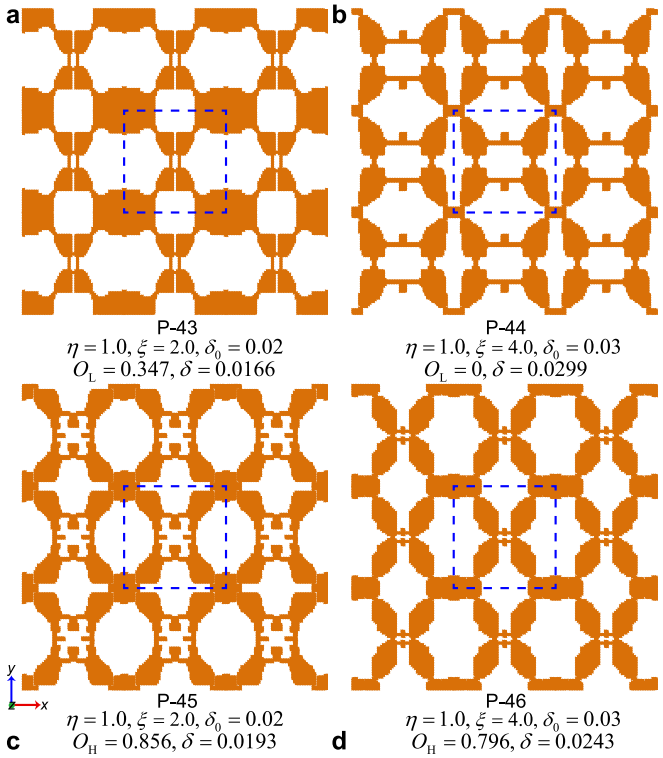

Fig. 16. Customized anisotropic square-lattice PMs. (a-b) Three 3 × 3 microstructures with their representative prescribed η, δ_0 and ξ using the low-order optimization. **(c-d)** Three 3 × 3 microstructures with their representative prescribed η, δ_0 and ξ using the high-order optimization. Dash line represents a C_{2v}-symmetry PM microstructure.

4.5. Anisotropic PMs with impedance matching and prescribed anisotropy

To explore the effect of combing all feature parameters, we adopt the integrated model in Eqs. (7)–(10) to seek broadband single-mode PMs with prescribed anisotropy degrees and impedance matching in a square lattice as shown in Fig. 16. For the same prescribed η, the microstructure shows reduced symmetry with the increase of the anisotropy degree. The considered four microstructures share common topological features: (1) four solid blocks at four corners, (2) four big blocks in the center, and (3) several slender rods. Compared with the low-order optimization results, the high-order optimization gives rise to wider single-mode frequency ranges for longitudinal waves. This signifies that, if one needs to concurrently consider the pentamode feature, prescribed mass density, perfect impedance matching and anisotropy degree, it is crucial to construct a weak anisotropic microstructure consisting of multiple big solid blocks and small lumps located on the slender rods to lower the rotational mode for the broadband single-mode of longitudinal wave. It should be emphasized that it is difficult to reach a high anisotropy while keeping the broadband single-mode nature and ideal impedance matching simultaneously. The feature parameters of Microstructures P-44 and P-46 show the limiting states suggested by the model in Eqs. (7)–(10) for the square lattice.

Unlike the low-order square-lattice microstructures in Fig. 9, the low-order triangle-lattice ones in Fig. 17 possess much broader single-mode frequency ranges of longitudinal wave. This demonstrates that the triangle-lattice microstructures can easily lower the transverse wave modes and raise the lower-order rotational modes simultaneously for obtaining low-frequency broadband pentamode properties. In particular, P-47 can exhibit ultra-broadband single-mode behavior up to 163.7%, which represents a record-breaking performance in the field of PMs. This microstructure is composed of two big solid blocks distributed in the left and right edges and four small blocks containing the holes located on the other four edges. The topological feature of P-47 is a brand-new basic configuration for ultra-broadband single-mode PMs in triangle lattice. With the same prescribed η, microstructures with more solid blocks usually lead to a larger anisotropy degree. Since the high-order P-50, P-51 and P-52 are completely different, it is therefore difficult, if not impossible, to realize broadband single-mode nature under different requirements of anisotropy degree by only using a single specific topological feature. Overall, a larger anisotropy will result in smaller O_L or O_H. Note that, for both square and triangle lattices, it may be impossible to realize the broadband single-mode property in the premise of perfect impedance matching and large anisotropy degree (>4.0) simultaneously. Of course, if the single-mode feature is ignored in the optimization, the optimization model could certainly realize a higher and even ultra-high anisotropy.

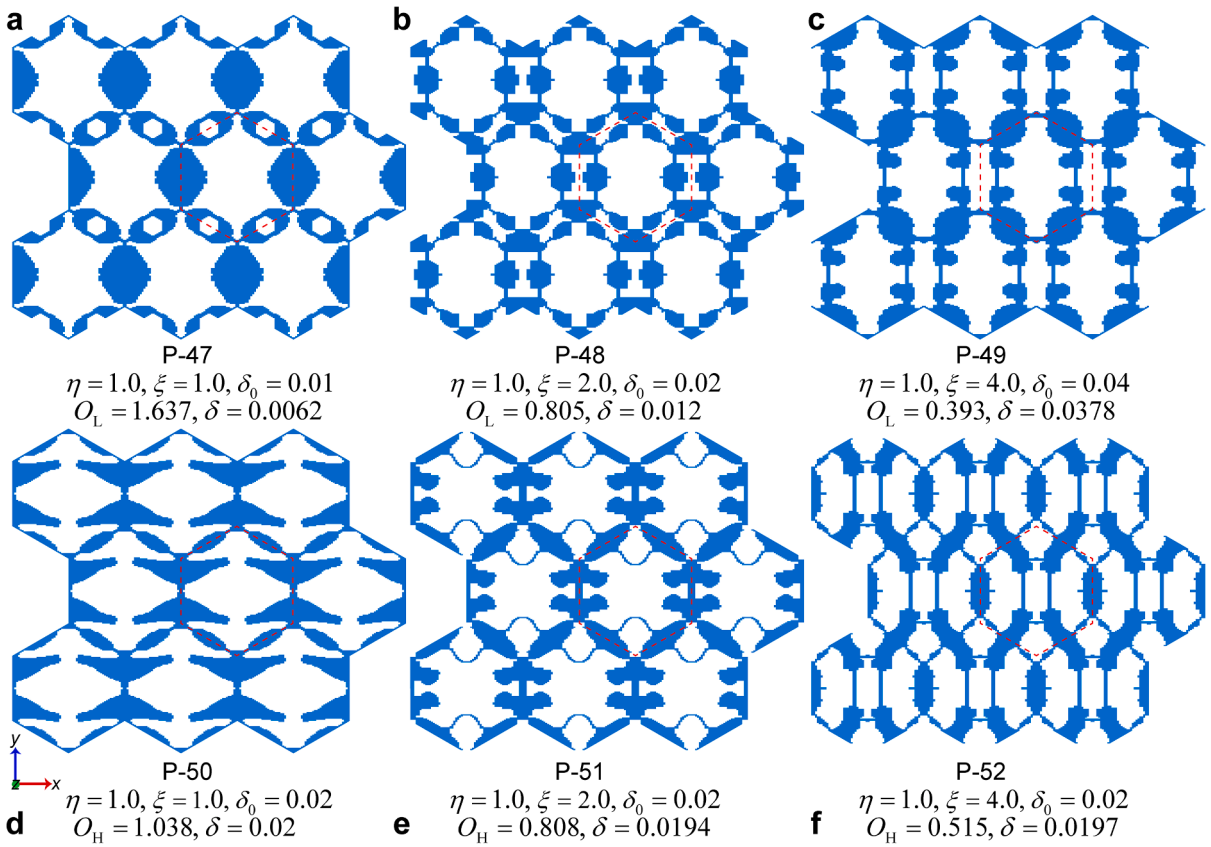

Fig. 17. Customized anisotropic triangle-lattice PMs. (a-c) Three 3 × 3 microstructures with their representative prescribed η, δ_0 and ξ using the low-order optimization. **(d-f)** Three 3 × 3 microstructures with their representative prescribed η, δ_0 and ξ using the high-order optimization. Dash line represents a C_{2v}-symmetry PM microstructure.

4.6. Mechanisms for broadband single-mode of exclusive longitudinal wave

To reveal the physical nature of the broadband single-mode of longitudinal waves for the aforementioned microstructures, we investigate the dispersion relations and the eigenstate modes at small wave vector point (ΓX/20) and high-symmetry wave vector points (X, Y and M) by choosing two representative inverse-designed Microstructures: P-29 and P-47.

To characterize the wave features, we mark the wave mode features of every energy bands by four different colors. The dispersion relations in Fig. 18(a) clearly show that P-29 indeed possesses a broadband single-mode between the second and third bands. Meanwhile, the longitudinal phase velocity keeps nearly constant, in complete agreement with water acoustic line. The modes in Fig. 18(b) at ΓX/20 point illustrate that the first- and the second-order components indeed display purely transverse and longitudinal wave motions. The fist-order modes at X, Y and M points show different polarized transverse wave features. However, the second-order modes at X, Y and M points and third-order mode at TX/20 point represent low-order rotational vibrations. The third-order modes at X, Y and M points show high-order rotational vibrations. Therefore, it is the multi-form and multi-order (low and high) rotational modes that give rise to the large mode bandgap for the rational-mode waves, thus avoiding the coupling with the longitudinal waves and generating broadband single-mode feature.

As for the low-order optimization case, we select P-47 to analyze its dispersion relations and eigenmodes in Fig. 19(a), and (b), respectively. It indeed shows single-mode feature of longitudinal waves with an ultra-broadband frequency range of [3376.7 Hz, 25,000 Hz], featuring a record-breaking relative bandwidth of 152.4%. The modes in Fig. 19(b) at TX/20 point show purely transverse and longitudinal wave features for the first and second bands. The first-order modes at X point show the lower-order rotational vibration. However, the fist-order modes at Y and M points show obvious strong anisotropic vibrations. The second- and the third-order modes at X, Y and M points illustrate strong anisotropic vibrations as well.

It should be noticed that the so-called “bandgap” appearing in the band structure of a PM is the mode bandgap other than full bandgap. A mode bandgap only applies to some specific wave modes, whilst a full bandgap implies a full stop band applicable to all possible wave modes. Generally speaking, the distinctive feature of a PM is exhibited in the mode bandgap where only a purely longitudinal wave mode appears, thus providing a mode bandgap for shear wave modes or mixed wave modes, whose position and width are related to the rotational vibration and shear vibration of the microstructure. In fact, some rotational vibrations can be coupled with the shear vibrations and thus lower the first shear band. Multiple anisotropic local vibrations can generate a large mode

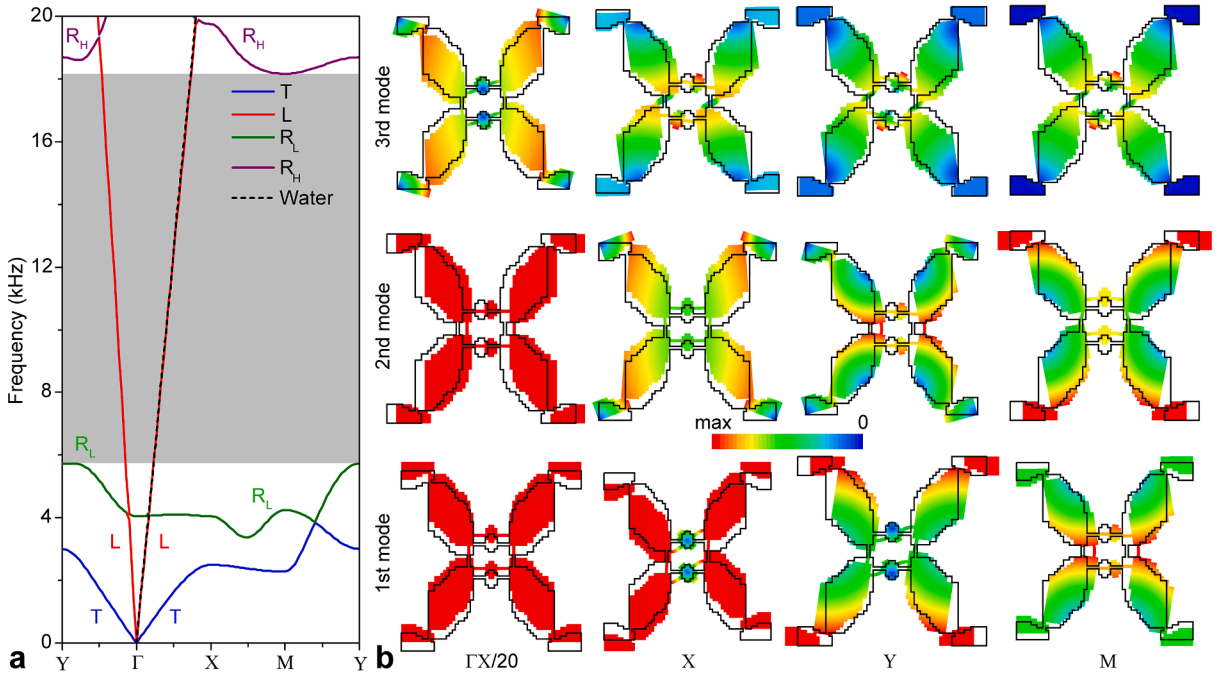

Fig. 18. Broadband single-mode mechanism for P-29. (a) Dispersion relation from Bloch-wave analysis. Shaded areas show the single-mode frequency range [5730.6 Hz, 18,163 Hz] which nearly perfectly match with water, featuring a relative bandwidth of 104.1%. **(b)** The Bloch modes of the lowest three bands at high-symmetry points (X, Y, and M) and small wave vector (ΓX/20) of the Brillouin zone shown in Fig. 1. Insets show the distributions of the magnitude of the modal displacement field. Letters of T, L, R_L and R_H represent the transverse, longitudinal, low-order rotational and high-order rotational modes, respectively. Dash lines are the dispersion curves of water.

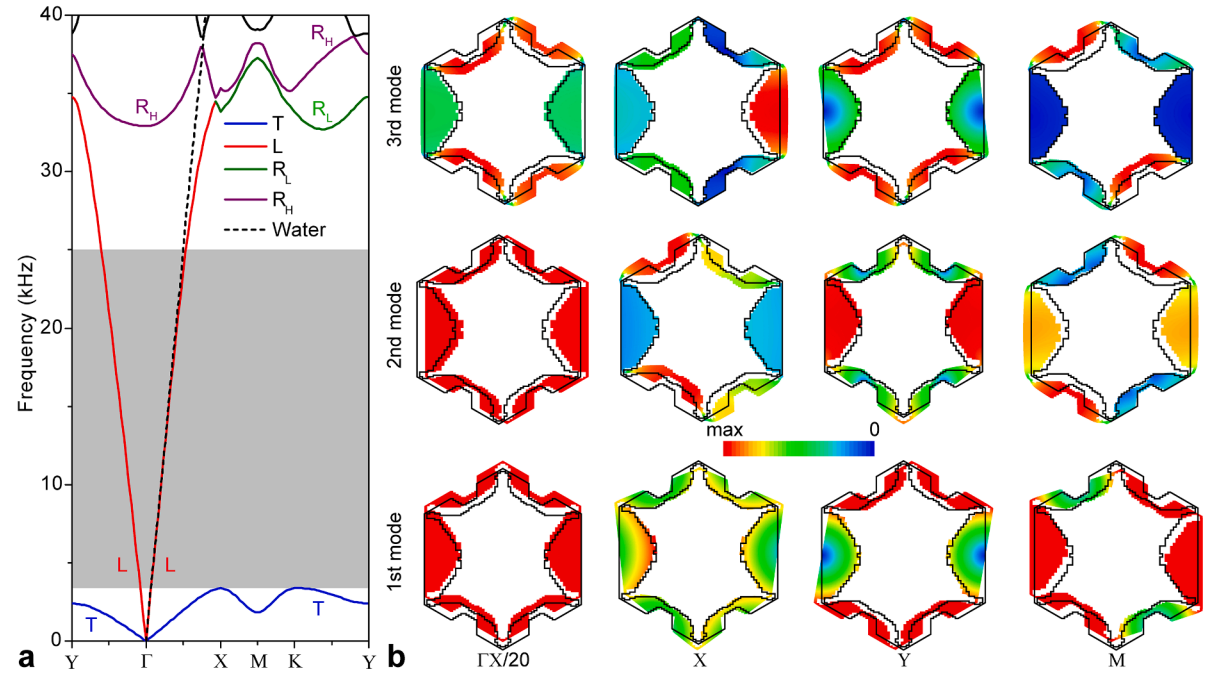

Fig. 19. Broadband single-mode mechanism for P-47. (a) Dispersion relation from Bloch-wave analysis. Shaded areas show the single-mode frequency range [3376.7 Hz, 25,000 Hz] which can be nearly perfectly matched with water, featuring the relative bandwidth of 152.4%. **(b)** Bloch modes of the three lowest bands at high-symmetry points (X, Y, and M) and small wave vector (ΓX/20) of the Brillouin zone shown in Fig. 1.

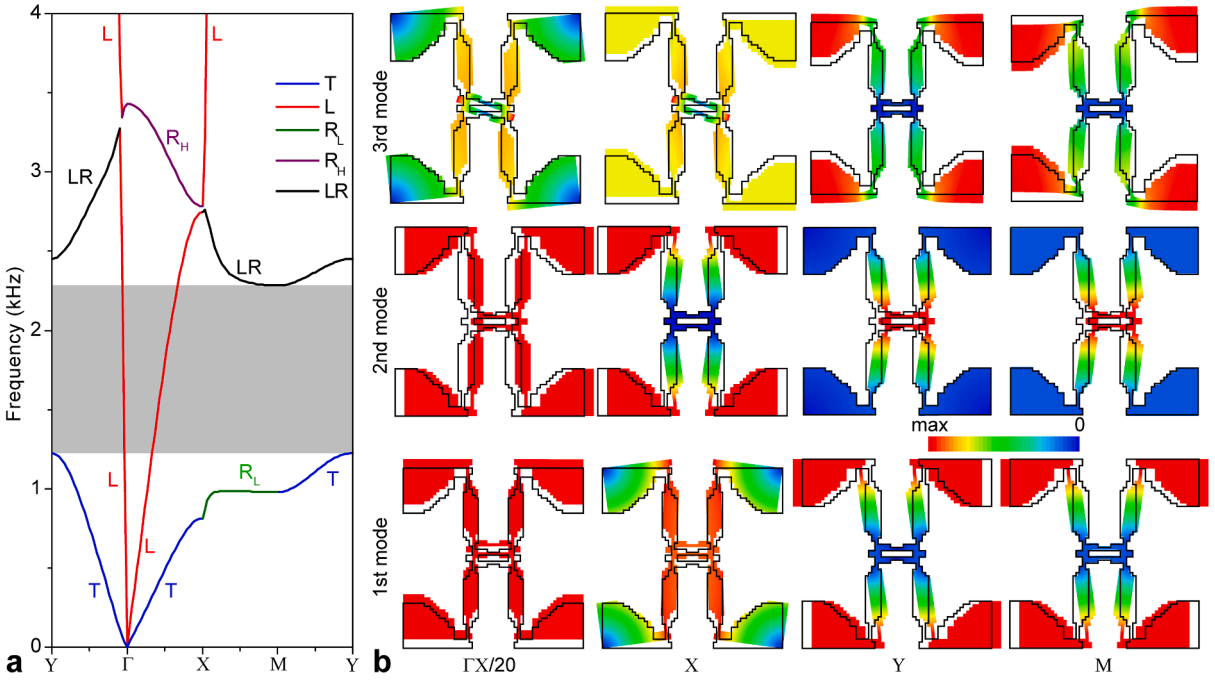

Fig. 20. Broadband single-mode mechanism for ultra-highly anisotropic P-39. (a) Dispersion relation from Bloch-wave analysis. Shaded areas show the single-mode frequency range [1223.9 Hz, 2283.3 Hz] which lead to the anisotropic extent as high as 100, featuring the relative bandwidth of 60.4%. **(b)** Bloch modes of the three lowest three bands at high-symmetry points (X, Y, and M) and the small wave vector (ΓX/20). Letter of LR represent the local resonance modes.

bandgap for the rotational vibrations and shear vibrations. So, we believe that the superposition of low-order rotational vibrations and multiple anisotropic local vibrations can give rise to the broadband single-mode feature.

In general, a three-phased matematerial like the sonic crystal proposed by Liu et al. (Science 289, 1734–1735, 2000) only exhibits a very narrow bandgap at low frequencies. However, a single-phased matematerial with pores, as the present PM, can offer very large bandgaps induced by different local vibrations (cf. Dong et al., 2014; ; Wang et al., 2014). For the lower edge of bandgaps, big blocks vibrate rather like rigid bodies, while slender rods acting as springs; for the upper-edge modes, while the slender rods vibrate, the blocks almost remain still. Similarly, large mode bandgaps for shear and mixed modes are also created by the present ortho-symmetric big solid blocks connected by slender rods.

To explain the broadband single-mode feature with high anisotropy, we present the dispersion relations and the eigenstate modes of Microstructure P-39 in Fig. 20. It is noted that a low-frequency single-mode range appears in the band structure. The modes in Fig. 20(b) at TX/20 point still show purely transverse and longitudinal wave features for the first and the second bands. But the fist-order modes at X, Y and M points show ultra-high anisotropic local vibrations. In addition, the fist-order mode at X point also contains low-order rotational vibration. The second-order modes at X, Y and M points and all the third-order modes show typical local resonances through the local vibrations of the big or small blocks. Accordingly, the superposition of the low-order rotational modes and multiple anisotropic local vibrations (Dong et al., 2014; Wang et al., 2014) can effectively lead to the broadband single-mode feature of the ultra-high anisotropic PMs.

4.7. Extracted simplified pentamode configurations

In an attempt to simplify the optimized configurations to facilitate the fabrication and guide the design of PMs, we select two most representative inverse-designed microstructures P-29 and P-47 to present simplified broadband single-mode PM microstructures and extract their dominant topological features, see Figs. 21 and 22. The simplified anisotropic broadband single-mode square-lattice microstructure mainly contains several big and small solid blocks with several slender rods. Fig. 21(b)–(e) show the effect of three dominant geometrical parameters (w_1, w_2 and h_1) on the resulting effective mass density, pentamode parameters (α, β) and the anisotropy degree. Fig. 21(b) shows that the simplified PM configuration can generate the wide range of mass density varying from 1000 to 2100 kg/m^3. The configuration can well grasp the perfect pentamode feature for $\alpha>0.988$ and $\beta<0.013$. In addition, the results in Fig. 21(f) show that the corresponding effective impedance can well match with water as well. However, the corresponding anisotropy degree has no significant change and keeps about 3.0. Fig. 21(g) further demonstrates the simplified model can bring about the anisotropy degree ranging from 5.2 to 84 under the new combination of three parameters (w_2, w_3, h_2). So, it is the difference between the width of the big solid block and the thickness of the narrow connecting rod that determines the anisotropy of the microstructure. This also means that, with suitable structural parameters, the simplified model retains the perfect impedance

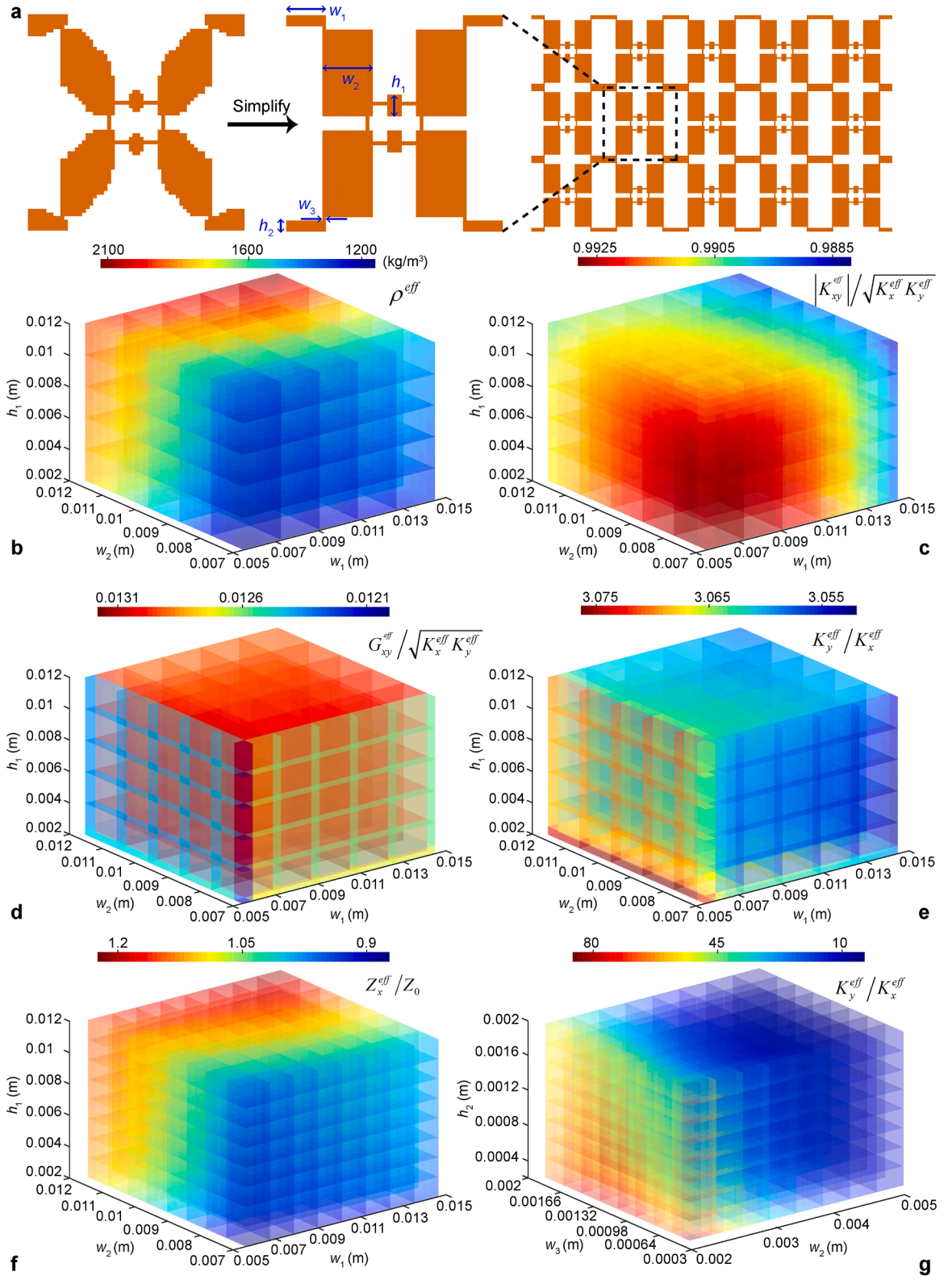

(caption on next page)

Fig. 21. Simplified anisotropic square-lattice PM. (a) A representative simplified anisotropic microstructure with multiple solid blocks originated from P-29. (b-f) Effective mass density (b), pentamode parameters $|K_{xy}^{eff}|/\sqrt{K_x^{eff}K_y^{eff}}$ (c) and $G_{xy}^{eff}/\sqrt{K_x^{eff}K_y^{eff}}$ (d) anisotropy degree K_y^{eff}/K_x^{eff} (e) and impedanceZ_x^{eff}/Z_0 (f) under the combinations of three dominated geometrical parameters w_1, w_2 and h_1 in (**a**). (g) Anisotropy degree K_y^{eff}/K_x^{eff} under the combinations of other three parameters w_3, w_4 and h_2 in (**a**).

matching, ideal pentamode feature and ultra-high anisotropy simultaneously.

Based on the triangle-lattice P-47 with the largest single-mode frequency range, we also present in Fig. 22(a) the corresponding simplified configuration which is composed of six big solid blocks located on the edges. Compared with the square-lattice configuration in Fig. 21, the triangle-lattice one is more favorable to smaller density varying from 645 to 1780 kg/m^3. In addition, it can possess the ideal pentamode feature with a α larger than 0.985 and a β smaller than 0.02 for most parameter combinations. As shown in Fig. 22(f), while the normalized impedance changes from 0.46 to 2.17, some parameter combinations can also maintain the acceptable value about 1.1. But its anisotropy in Fig. 22(e) is almost unchanged at about 1.0 for all combinations. However, as shown in Fig. 22(g), constructing the microstructure with the other three feature parameters (w_3, w_4, R) can also lead to strong anisotropy ranging from 0.04 to 3.5. Therefore, the difference between the thicknesses of the outer frame along the two principle directions mainly determines the anisotropy degree. In general, the two simplified configurations in Figs. 21 and 22 can represent the perfect pentamode feature and provide a useful design space for large range of mass density and anisotropy.

The two categories of simplified configurations in Figs. 21 and 22 can well maintain the broadband single-mode pentamode feature while keeping the ideal impedance, high anisotropy and large-scale mass density, irrespective of how dominant parameters change. Certainly, different categories of inverse-designed microstructures can be used as novel elements to guide the systematic design of new high-performance PMs with customized properties.

5. Water-like wave characteristics of topology-optimized PMs

To demonstrate the water-like wave characteristics of our optimized microstructures, we examine the wave propagation in four representative Microstructures P-14, P28, P20 and P-31 in water as shown in Fig. 23. Fig. 23(b) shows that P-14 behaves like water in Fig. 23(a) from the subwavelength (2000 Hz, λ=25a) to short subwavelength scale (7000 Hz, λ=7.14). Two square-lattice microstructures in Fig. 23(b) and (c) clearly show the perfect water-like behavior without any reflection within the broadband range. The acoustic waves maintain perfectly plane while the displacement distributions in the PMs also display classical longitudinal wave feature. The performance of P-28 in Fig. 23(c) implies that the microstructure can still behave the broadband water-like nature even with a mass density much smaller than water. Similarly, Fig. 23(d) and 23(e) illustrate that the high-symmetric triangle-lattice can also allow for perfect acoustic wave manipulation. In particular, P-31 can be perfectly matched with water even at the ultra-high frequency of 19 kHz. Therefore, for both low-frequency and ultra-high-frequency ranges, the inverse-designed microstructures can steadily behave as metafluids along the x-direction.

In theory, if a pentamode microstructure of finite size cannot satisfy all physical requirements simultaneously, scattering would occur. To verify the water-like performance of the microstructures in this case, Fig. 24 presents the steady responses and the corresponding total scattering section (TSCS) (Layman et al., 2013) for representative Microstructures P-14, P-29, P-20 and P-47 under incident plane waves. It can be seen that these four representative microstructures exhibit rather low scattering below 15 kHz (TSCS<0.2), preserving the propagating wavefront of plane waves, despite the existence of the PMs. However, for very high frequencies, Fig. 24(b) and (d) show strong scattering. This is because the subwavelength effective medium theory is no longer valid to characterize the pentamode feature at high frequencies. In addition, the anisotropic P-29 shows relatively stronger scattering than the other isotropic ones. This means that the anisotropy can compromise the matching with water to a certain extent.

Overall, most optimized microstructures reported in the present paper can not only perfectly match with water but also maintain excellent low scattering property below 15 kHz, even for PMs with a finite size. Therefore, from either macroscopic or microscopic perspectives, the wave feature of the designed microstructures is perfectly compatible with water. In fact, this nearly perfect property attributes to their broadband single-mode feature. Otherwise, a strong wave scattering would have been induced when placing a finite PM in water (Cai et al., 2016).

6. Pentamode metasurfaces converting propagating waves to evanescent surface modes

To further demonstrate the practical value of the inverse-designed PMs, we combine the concept of pentamode with that of the metasurface which can support the extreme beam-steering ability for solving typical engineering applications, such as low-frequency and broadband acoustic shielding as shown in Fig. 25(a). By converting the propagating waves into evanescent mode over the surface, a properly designed PM device is expected to effectively shield the multiple-wavelength noise from a base/equipment. The PM metasurface we designed is composed of an array of PM microstructures in square lattice. As shown before, the C_{2v}-symmetry provides a large design space and excellent pentamode features simultaneously. Each microstructure with the prescribed C_{2v}-symmetry topology is generated through topology optimization. Because the optimized microstructures contain many holes, we have to make some small solid regions undesignable in topology optimization to ensure the connectivity among different microstructures along the x-direction. Through inverse-design, we expect to discover novel configurations and provide a systematic framework for realizing

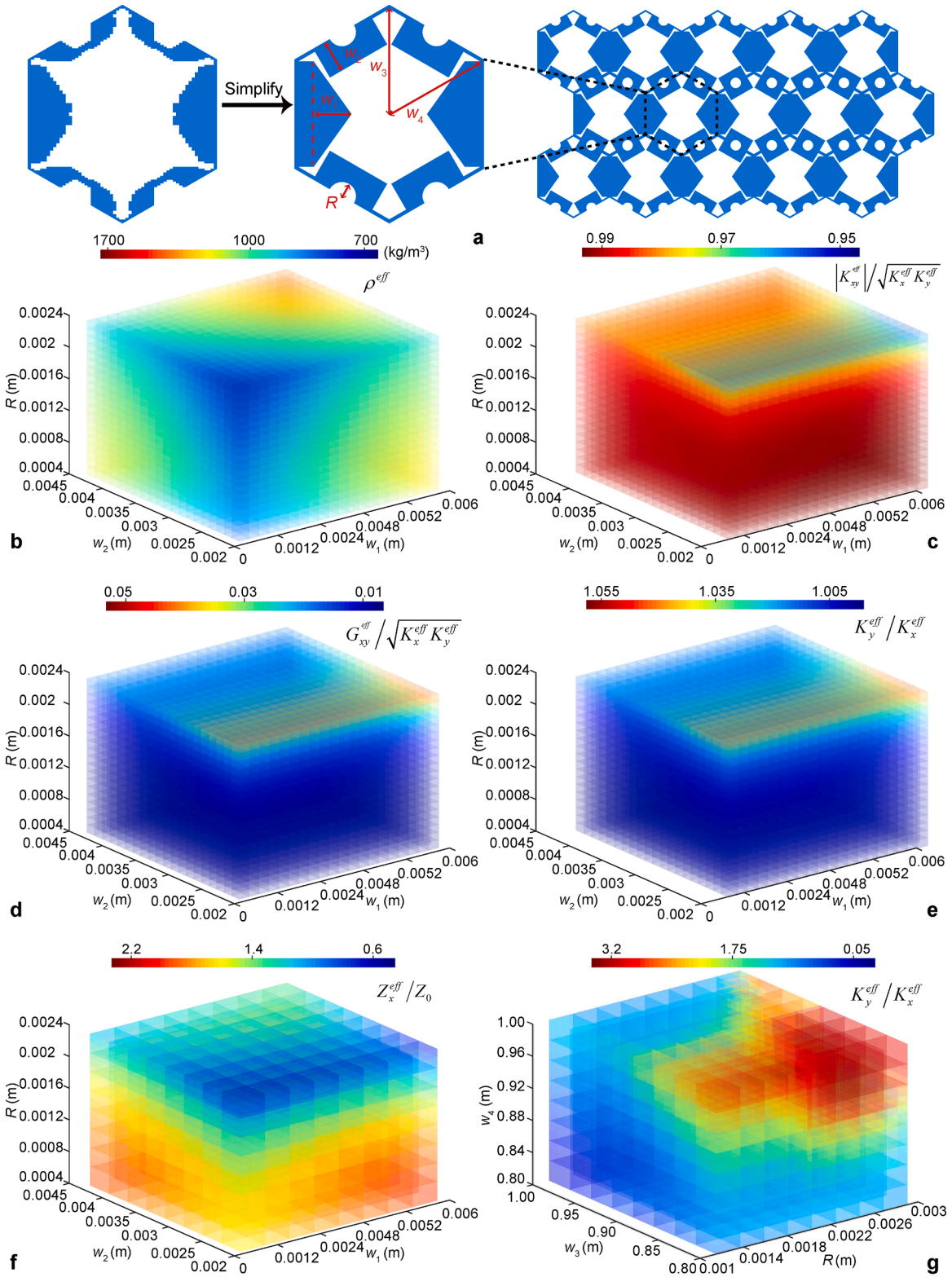

(caption on next page)

Fig. 22. Simplified anisotropic triangle-lattice PM. (a) A representative simplified anisotropic microstructure with multiple solid blocks originated from P-47. (b-e) Effective mass density (b), pentamode parameters $|K_{xy}^{eff}|/\sqrt{K_x^{eff}K_y^{eff}}$ (c) and $G_{xy}^{eff}/\sqrt{K_x^{eff}K_y^{eff}}$ (d) anisotropy degree K_y^{eff}/K_x^{eff} (e) and impedance Z_x^{eff}/Z_0 (f) under the combinations of three dominated geometrical parameters w_1, w_2 and R in (**a**). (g) Anisotropy degree K_y^{eff}/K_x^{eff} under the combinations of other three parameters w_3, w_4 and R in (**a**).

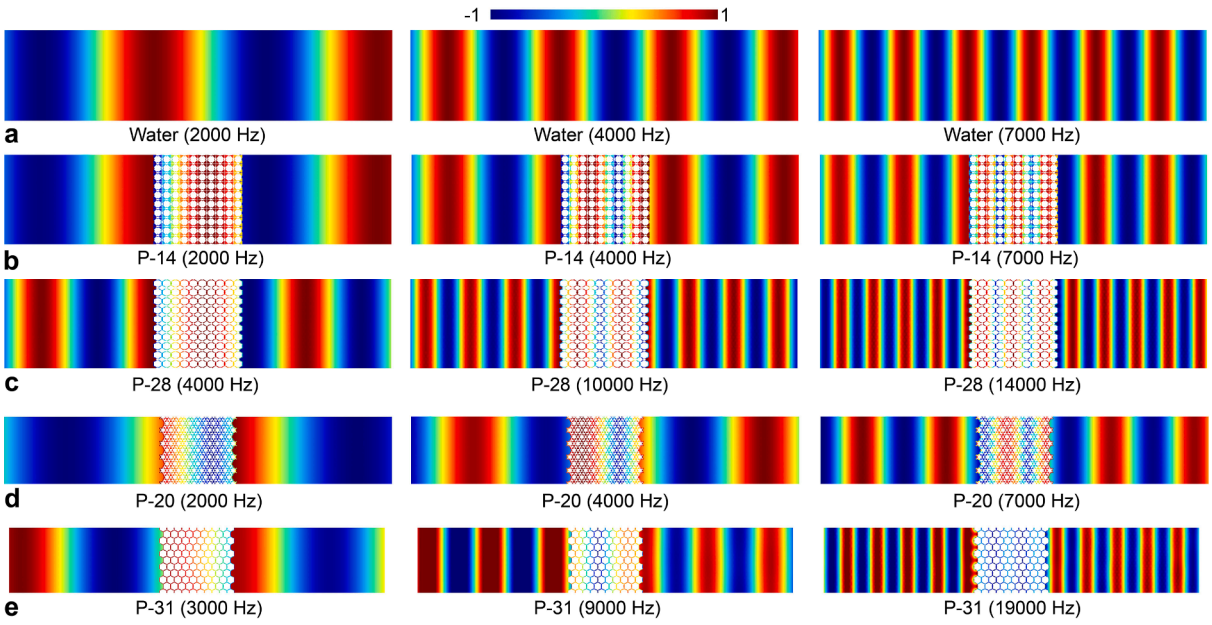

Fig. 23. Underwater acoustic wave propagation through four representative PMs. (a-b) Pressure fields under incident acoustic plane waves from water for square-lattice P-14 and P-28. The pressure fields for water at different frequencies are also presented. **(c-d)** Pressure fields under incident acoustic plane waves from water for the triangle-lattice P-20 and P-31. Periodic boundary conditions are imposed on the upper and lower edges of the simulation models. The left and right boundaries of the model adopt nonreflecting boundary condition. Typical fluid-solid coupling boundary condition is applied on the interface between the PMs and water. The colors within the PMs show the displacement fields.

arbitrary and rigorous index in the underwater acoustic environment.

To solve the inverse problem illustrated in Fig. 25, we implemented again a novel inverse-design strategy to generate the customized pentamode microstructures under specific macroscopic distribution. Since most microstructures need to possess very large effective indices, we have performed abundant optimization tests but found it impossible to make a microstructural match with water and equipped with the broadband single-mode property simultaneously. Particularly, the periodic distribution of the microstructures can make the PM device difficult to excite other complex modes besides the longitudinal waves. As an alternative, it is more feasible to make the longitudinal phase velocity close to the theoretical one in the low-frequency range. Another key point is to ensure the consistency between the effective longitudinal moduli along two principle directions. This is due to the fact that the PM device will generate apparent scattering if the two principle moduli are different when propagating waves along one principle direction are converted into the waves along the other principal one. Therefore, it is necessary to guarantee that both principle longitudinal moduli are nearly the same. As a result, the unified optimization problem for creating a pentamode metasurface microstructure with the customized wave motions within a broadband and low frequency regime is defined by

$$For:\ \Omega_D = [\rho_1,\ \rho_2,\ \rho_3 \cdots \rho_i],\ (i = 1,\ 2, \cdots N \times N), \tag{19}$$

$$Maximize:\ O(\Omega_D) = -|a\omega_{x3}/\pi - c_{LT}| \tag{20}$$

$$\begin{aligned} Subject\ to:\ & \min_{\Omega_D}(\boldsymbol{w}) \geq w_0, \\ & \delta(\Omega_D) = -max\left(\delta_{K_{xy}},\ \delta_{G_{xy}},\ \delta_{Z_x},\ \delta_\rho,\ \delta_{Ani}\right) \geq \delta_0, \\ & \rho_{(N/2-1)} = 1,\ \rho_{(N/2)} = 1,\ \rho_{N\times(N/2-1)} = 1,\ \rho_{N\times(N/2)} = 1, \end{aligned} \tag{21}$$

where ω_{x3} is the third eigenfrequency at X point; w_0 is set at $a/60$; δ_0 at -0.02; $\rho_{(N/2-1)}$, $\rho_{(N/2)}$, $\rho_{N\times(N/2-1)}$, $\rho_{N\times(N/2)}$ are the four fixed pixels shown in Fig. 25(b); and c_{LT} denotes the longitudinal phase velocity which is given by (Tian et al., 2015)

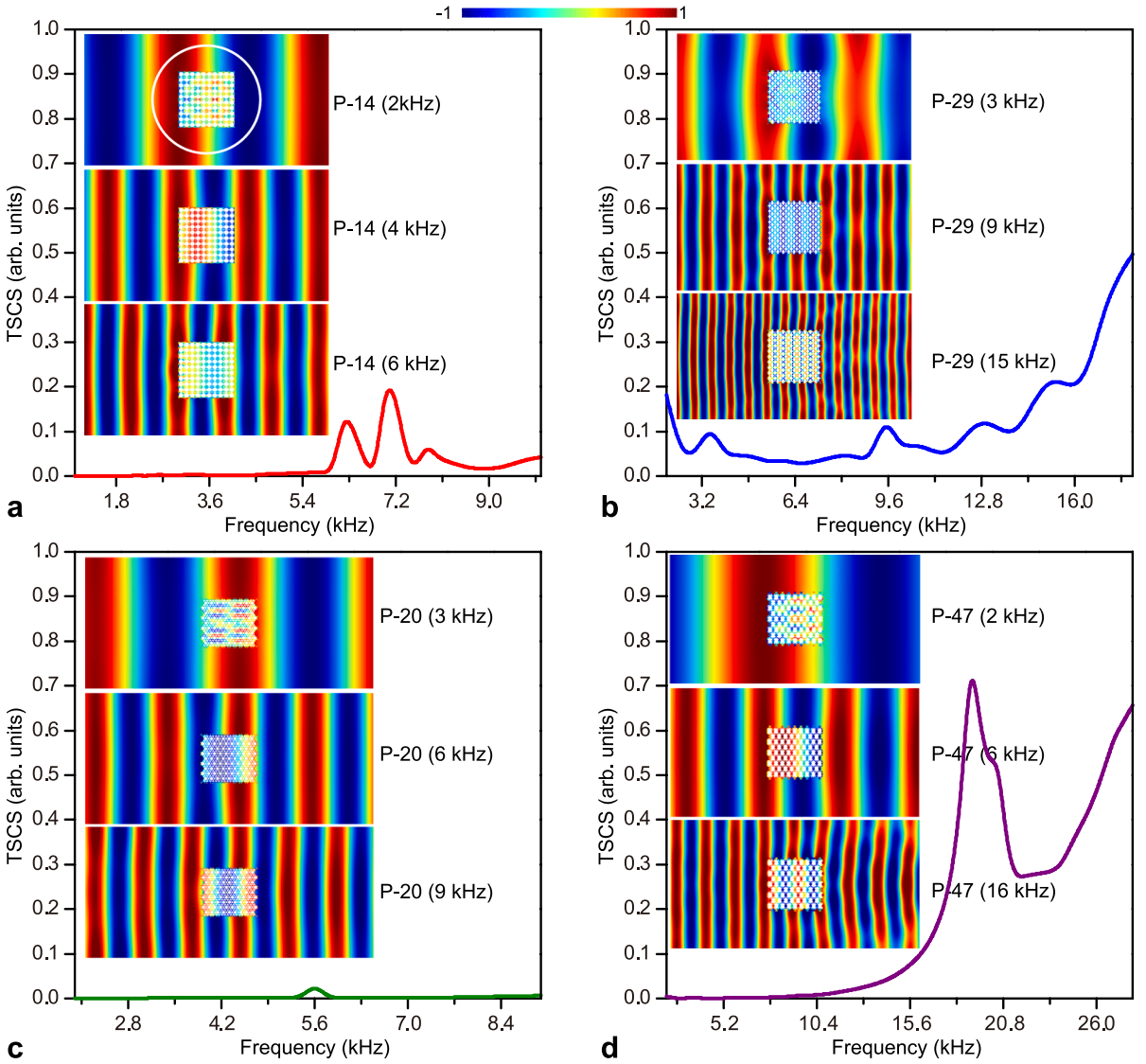

Fig. 24. Scattering characterization of representative PMs. (a-d) Total scattering cross section (TSCS) for the square-lattice and triangle-lattice PMs (a: P-14, b: P-29, c: P-20, d: P-47) as a function of the operating frequency. Pressure fields at several representative frequencies are also presented. Nonreflecting boundary conditions are imposed on the outer edges of the model. Typical fluid-solid coupling boundary conditions are applied at the interface between the PMs and water. White circle in (**a**) denotes the integration region for calculating the TSCS.

$$\frac{1}{c_{\mathrm{LT}}(x)} = \frac{1}{Hc_0}\int \sin\theta_t(x)dx, \tag{22}$$

where H is the thickness of the metasurface along wave propagation direction (y-direction); θ_t denotes the refraction angle of waves which is selected as 90-degree herein. In view of the required perfect impedance matching, the ideal mass density of the microstructure is defined as $\rho(x)=\rho_0 c_0/c_{\mathrm{LT}}(x)$. Then η can be determined by $\eta=c_0/c_{\mathrm{LT}}(x)$.

Based on the above framework, we obtain an inverse-designed broadband acoustic device comprising a series of customized square-lattice C_{2v}-symmetry PM microstructures, see Fig. 26. Due to the subwavelength thickness along the propagation direction (y-direction), this kind of functional device in Fig. 26(a) is simple and easy to be integrated for practical applications. This device is composed of a cluster of microstructures symmetric about y-axis. In this case, the macroscopic gradient phase change can cause a notable variation of the wavefronts. Except M4, other microstructures share the common topological feature: four big solid blocks on the edges; and four small blocks adhered to four slender rods. For Microstructure M4 with a small mass density under a large porosity, the upper and the lower big blocks are replaced by slender rods. Moving away from the center, the effective mass densities of the Microstructures M1-M3 gradually increase. But the density of M-4 suddenly reduces before it starts increasing again from M4-M10. In fact, the microstructures with multiple symmetric solid blocks and narrow connectors in Fig. 26(b) and (c) are broadly similar with the inverse-

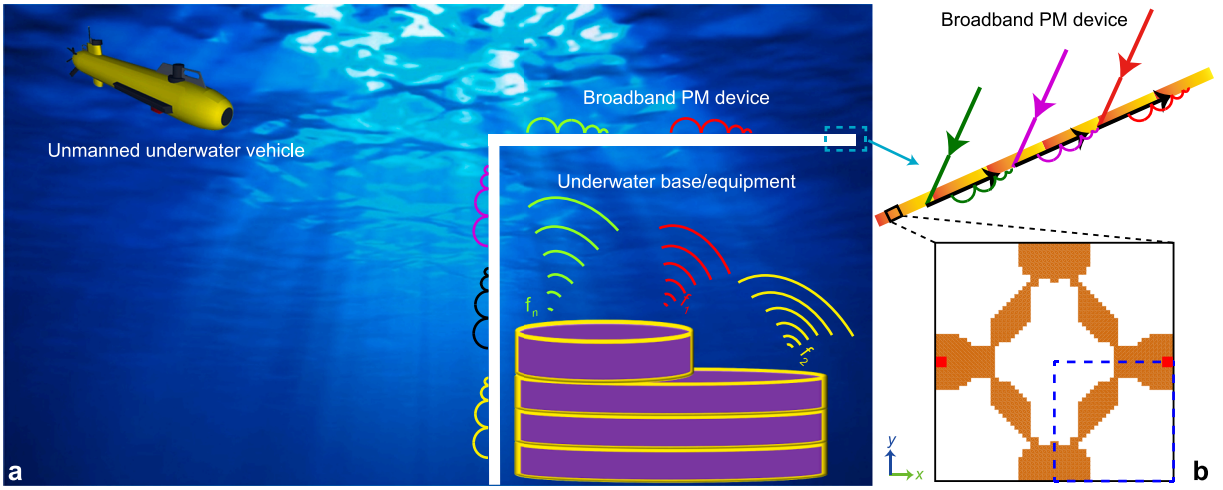

Fig. 25. Schematic of an inverse-designed broadband underwater device for acoustic shielding in an engineering sense. (a) The underwater multi-wavelength noise from the base/equipment can be isolated by the PM device. **(b)** Schematic of a broadband customized PM device on demand based on the phase-gradient concept. Incident acoustic waves are converted into evanescent surface wave mode. The metasurface is composed of a cluster of customized C_{2v}-symmetry PM microstructures. Regions surrounded by the dash lines denote the reduced design domain in topology optimization. Note that the pixels marked by red squares are fixed in topology optimization.

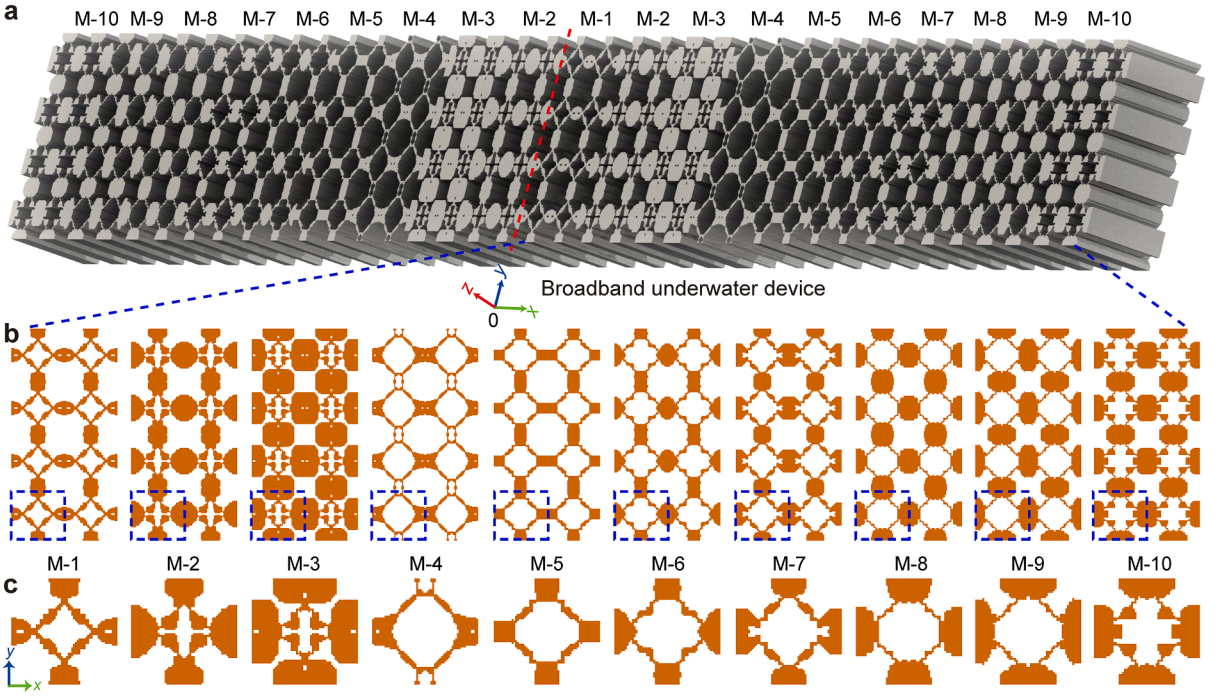

Fig. 26. Inverse-designed broadband underwater device based on customized PMs. (a) Broadband underwater device (1.14 m × 0.12 m × 0.15 m) composed of 38 × 4 topology-optimized PM microstructures. Ten microstructures (M1-M10) distribute along the x-direction. Each pentamode macrostructure consists of 2 × 4 microstructures. **(b)** Ten 2 × 4 PM lattice structures. The dashed part shows the corresponding microstructure of each macrostructure. **(c)** Topology-optimized C_{4v}-symmetry pentamode microstructures (M1-M10) in the square lattice with prescribed effective intrinsic parameters. Note that M1-M3 are made of aluminum while the other seven ones (M4-M10) are made of lead.

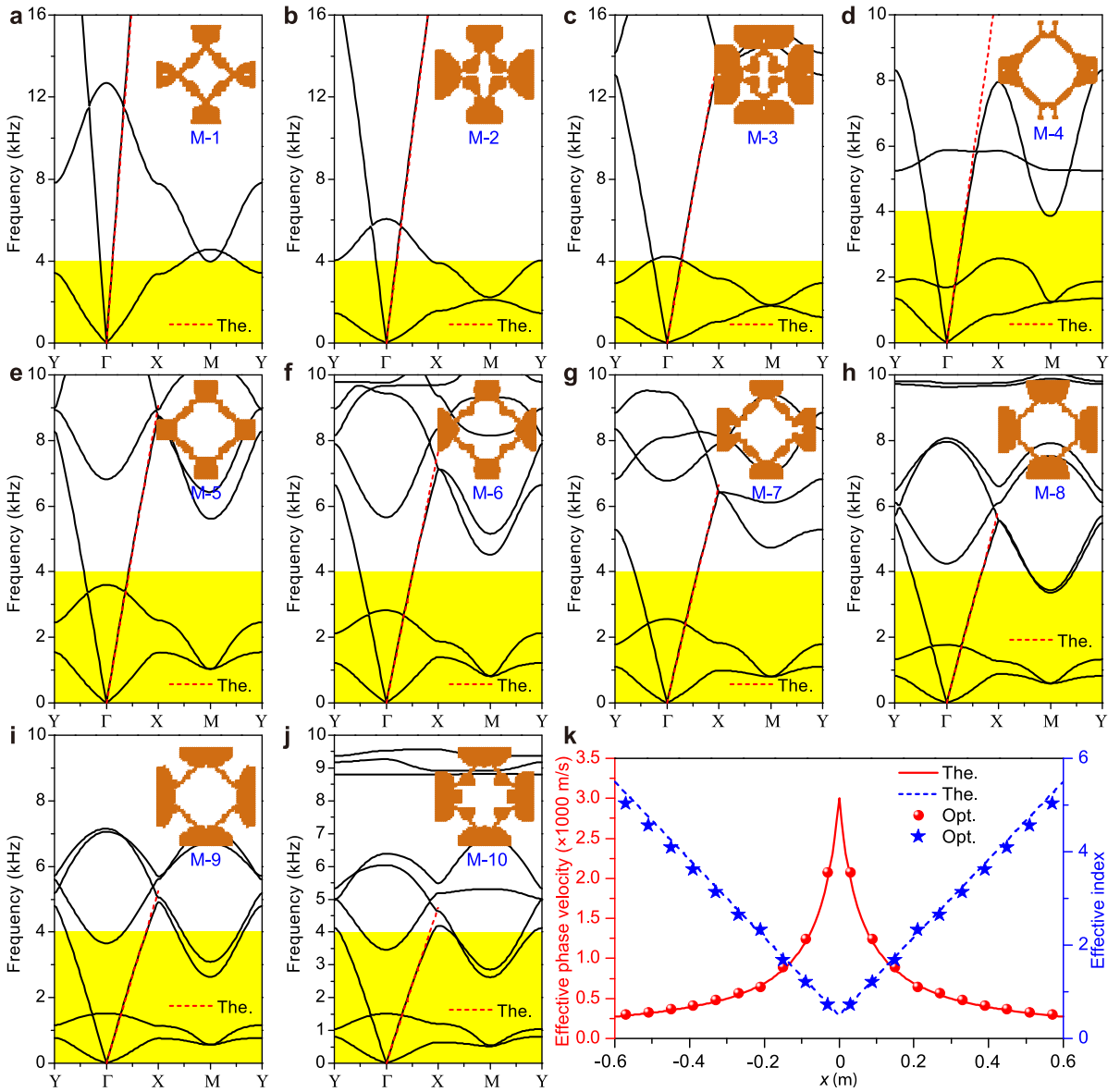

Fig. 27. Characterizations of pentamode metasurface microstructures. (a-j) Dispersion relations of topology-optimized microstructures with customized effective intrinsic parameters. Dashed lines denote the theoretical dispersion relation (The.) corresponding to the ideal metafluid with desired effective parameters. Shadow regions depict the resulting broadband range of the underwater device shown in Fig. 25(a). **(k)** Theoretical (The.) effective intrinsic parameters for broadband underwater acoustic device in Fig. 25 and optimized (Opt.) effective longitudinal phase velocities and effective indices of M1-M10 in Fig. 26. Ten discrete circles and stars with increasing *x*-values in the range of [0, 0.6 m] represent the parameters of M1-M10, respectively. Similarly, symmetric circles and stars show the values for the same microstructures left to the device center.

designed ones in the previous sections. However, there are many significant differences between the two cases because of the involvement of more mechanical and structural properties. This again indicates that a systematic inverse design is indispensable.

To verify the correctness of the microstructures in Fig. 26, the dispersion relations of M1-M10 are shown in Fig. 27(a)–(j). Because of the similar topological features, these microstructures possess similar dispersions. Due to the direct correlation between effective index, mass density and phase velocity, the required index and mass density can be derived from the calculation of phase velocity using Eq. (22). In order to satisfy the rigorous effective index of 0.75, 1.25, 1.75, 2.25, 2.75, 3.25, 3.75, 4.25, 4.75, and 5.25, M1-M10 low down the transverse and the first-order longitudinal wave modes, exhibiting ideal pentamode feature for obtaining the expected phase velocity. We note that the very straight lines of longitudinal phase velocities perfectly match with the theoretically predicted velocities. This represents the key property for the acoustic control. We find that, except M-1, the other nine microstructures can give rise to single-mode in certain frequency ranges, although the single-mode nature is not explicitly considered in the optimization. Since the resulted bandwidth of the device depends on the range of the microstructure with the largest index (M-10), the exact working range

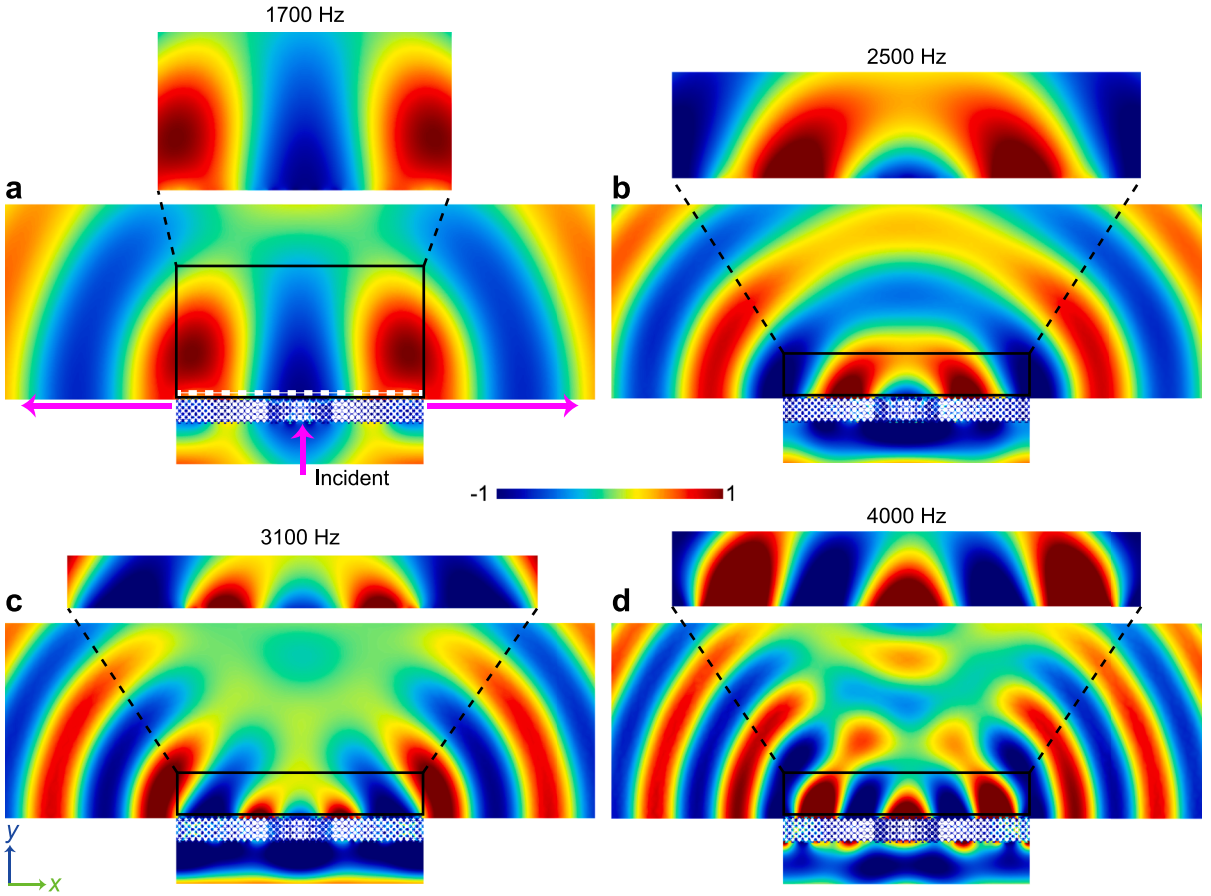

Fig. 28. Broadband underwater wave manipulation using inverse-designed metallic PM device surrounded by water. Acoustic pressure fields of inverse-designed PM device in Fig. 26(a) at the different frequencies are shown respectively. When the acoustic plane wave is incident upon the bottom edge of the PM device, the refracted waves are perfectly converted into evanescent surface mode from 1700 Hz to 4000 Hz. Energies from the evanescent waves propagate in free water region along the −90 and 90-degrees. Nonreflecting boundary conditions are imposed on the outer edges of the model. Typical fluid-solid coupling boundary conditions are applied at the interface between the device and water.

should be about [0, 4000 Hz]. In addition, Fig. 27(k) clearly demonstrates that the optimized features are highly consistent with the theoretical ones.

As a final assessment, of the premeditated wave functionality of the device in Fig. 26(a), we place it in water and examine the steady-state wave response under an low-frequency incident plane acoustic wave below the device, see Fig. 28. It follows that the refracted wave becomes evanescent wave along the surface of the device. Due to the perfect impedance matching, there is almost no reflected wave observed. In addition, the evanescent surface wave can reach the free acoustic field and propagate along the metasurface in water. This subwavelength evanescent wave manipulation can be observed at different frequencies. Moreover, the simulations also demonstrate that no noticeable scatting is solicited, which implies that the microstructures are indeed able to suppress possible transverse and bending modes.

To quantitatively characterize the refracted wave and validate its evanescent nature on the metasurface, we further study the scattering properties of the acoustic fields in Fig. 28 at four representative frequencies by extracting the simulated acoustic fields and then evaluating the diffraction orders. Energy amplitude distribution in each direction is obtained by performing Fourier transform (Li et al., 2018) along the dash line shown in Fig. 28(a). For all simulated results in Fig. 29, the inverse-designed device clearly induces the evanescent wave modes, i.e., nearly total energy is localized in the −1 order and +1 order directions (−90-degree and 90-degree) while other diffraction modes are almost completely suppressed. As a result, the wave vector component perpendicular to the surface has the imaginary value of $k_y = i\sqrt{k_x^2 - k_0^2}$ for $k_x \geq k_0$. The energy of the 0 order (0-degree) is very small compared with −1 order and +1 order ones, in agreement with the visualized acoustic fields in Fig. 28. Interestingly, the optimized results are better than the theoretical ones. It can be surmised that compared with the theoretical model based on a homogeneous medium, the introduction of a graded array of subwavelength microstructures can improve the diffraction resolution of the waves. That is, the device indeed converts the incident propagating wave into the evanescent surface mode. Because of the free acoustic field surrounding the device, energy generates obvious propagating mode in water. Therefore, it is the elaborately inverse-designed PM device that makes this kind of extreme

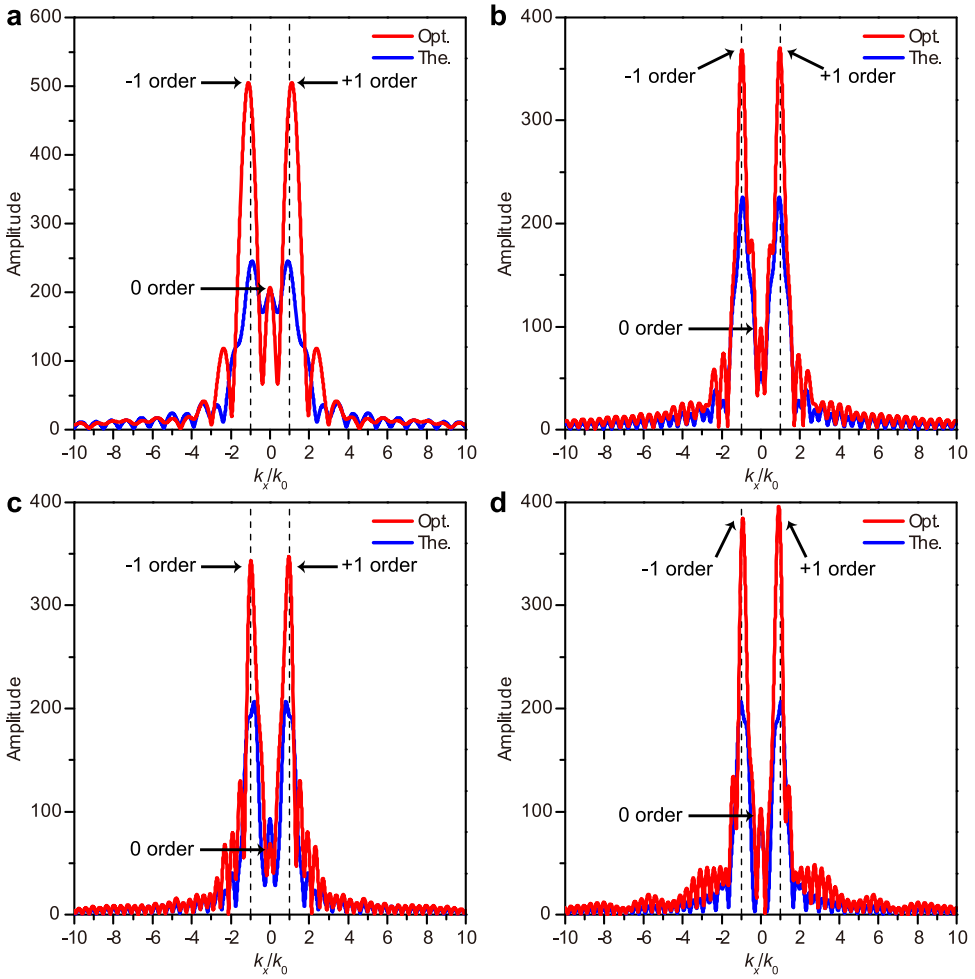

Fig. 29. Spatial Fourier transform of the simulated near-field pressure along the inverse-designed PM device. (a-d) The amplitude profiles of the transformed acoustic pressures extracted from the dash line above the metasurface in Fig. 28(a) at 1700 Hz (a), 3100 Hz (b), 3700 Hz (c) and 4000 Hz (d). The red and blue lines show the performances using the optimized metasurface (Opt.) and the theoretical medium (The.), respectively. Different amplitude peaks are marked by 0, −1 and +1 orders for the optimized results, respectively.

underwater acoustic beam steering possible in the low-frequency and broadband range.

7. Conclusions

In this paper, we propose a novel and systematic inverse-design strategy to design and construct customized isotropic and anisotropic PM microstructures on demand using a bottom-up topology optimization approach. Benefiting from the universality of the optimization model, several brand-new PM microstructures, under the assumption of C_{2v}, C_{4v} and C_{6v} symmetries in both square and triangle lattices, are discovered, which can deliver diverse prescribed combinations of properties such as mass density, structural symmetry, broadband, single-mode of longitudinal waves, isotropic, anisotropy degree or perfect impedance matching in both square and triangle lattices. Subsequently, we discover typical common topological features shared by these microstructures, i.e., multiple symmetric solid blocks connected with each other through slender rods. In addition, we reveal that the multiform and multiple-order rotational vibrations or the superposition of the low-order rotational vibrations and anisotropic local resonances can give rise to single-mode feature with large relative broadband (>100%) and even ultra-broadband (>150%) ranges. Moreover, most inverse-designed microstructures can exhibit perfect water-like wave properties and very weak scattering within broadband frequency ranges. On top of the microstructural design, we further propose a novel inverse-design strategy to create a low-frequency and broadband PM device for underwater acoustic shielding. A series of new microstructures with the multiple solid blocks and slender rods can behave like perfect metafluids with the prescribed effective indices. As a result, the assembled PM device allows for the conversion of propagating acoustic waves to the evanescent surface mode within [1000, 4000 Hz], realizing the low-frequency and broadband acoustic shielding of the underwater base/equipment. The proposed inverse-design models, novel PM microstructures, discovery of the underlying mechanisms of broadband single-mode and underwater high-performance PM device lay the foundation for large-scale and

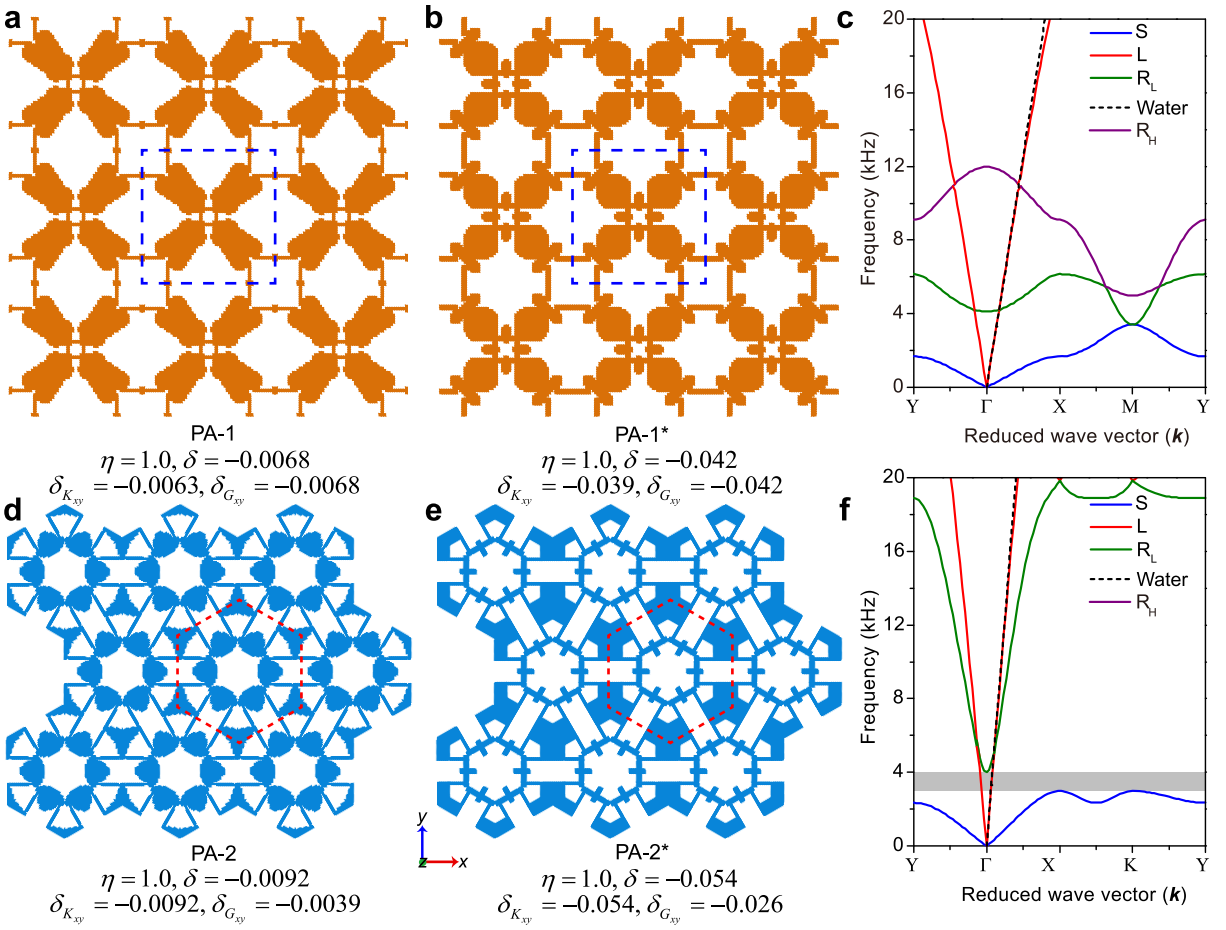

Fig. A1. Isotropic PMs with single pentamode features. (a-b) Three 3 × 3 square-lattice microstructures with the representative prescribed η. PA-1 and PA-1* are generated by the optimization with the minimal solid size w_0 of $a/60$ and $a/30$, respectively. (**c**) Dispersion relation from the Bloch-wave analysis for PA-1. **(d-e)** Three 3 × 3 triangle-lattice microstructures with the representative prescribed η. PA-2 and PA-2* are generated by the optimization with w_0 of $a/60$ and $a/30$, respectively. (**f**) Dispersion relation from the Bloch-wave analysis for PA-2. Notations of T, L, R_L and R_H represent the transverse, longitudinal, low-order rotational and high-order rotational modes, respectively.

integrated acoustic engineering using the PMs.

As a final remark, combing the proposed methodology with more advanced numerical or information technology such as deep learning algorithms is expected in our future work. This shall make the digital and customized design of 2D and even 3D PM devices possible, which will be a giant leap forward as a transition from proof-of-concept designs to practical applications of pentamode technology.

CRediT authorship contribution statement

Hao-Wen Dong: Conceptualization, Methodology, Formal analysis, Visualization, Writing – original draft. **Sheng-Dong Zhao:** Formal analysis, Data curtion, Validation. **Xuan-Bo Miao:** Data curtion, Validation. **Chen Shen:** Formal analysis, Data curtion. **Xiangdong Zhang:** Formal analysis. **Zhigao Zhao:** Formal analysis. **Chuanzeng Zhang:** Discussion, Writing – review & editing. **Yue-Sheng Wang:** Supervision, Writing – review & editing, Project administration. **Li Cheng:** Supervision, Writing – review & editing, Project administration.

Declaration of Competing Interest

The authors declare that they have no known competing financial interests or personal relationships that could have appeared to influence the work reported in this paper.

Acknowledgments

This work was supported by the Research Funds of the Maritime Defense Technologies Innovation, the National Natural Science Foundation of China (Grant Nos. 11802012, 11972646, 11991031, 11991032, 11902171 and 11534013), the Hong Kong Scholars Program (No. XJ2018041), the Postdoctoral Science Foundation (2017M620607), the Sino-German Joint Research Program (Grant No. 1355) and the German Research Foundation (DFG, Project No. ZH 15/27–1). H. W. Dong likes to thank Dr. Yi Chen (Karlsruhe Institute of Technology, Germany) for his helpful discussions.

Appendix A. Isotropic PMs by the optimization of single pentamode feature

In general, most common PMs only require the pentamode features. So it is effective and simple to design the microstructure with only two pentamode features by topology optimization which can be described by

$$\begin{aligned} &Maximize:\ O(\Omega_{\mathrm{D}}) = \delta(\Omega_{\mathrm{D}}) = -max\left(\delta_{K_{xy}},\ \delta_{G_{xy}}\right), \\ &Subject\ to:\ \min_{\Omega_{\mathrm{D}}}(\boldsymbol{w}) \geq w_0. \end{aligned} \tag{A1}$$

As a typical example, this optimization model can give rise to the desired PM with only two pentamode features ($\alpha\approx1, \beta\approx0$). Fig. A1 illustrates the novel isotropic C_{4v}-symmetry and C_{6v}-symmetry PM microstructures with the prescribed quasi-static mass density. Fig. A1(a) and (d) show the microstructures with $w_0=a/60$. To check the effect of w_0 on the optimization, Fig. A1(b) and (e) present the microstructures with $w_0=a/30$. Clearly, two square-lattice PA-1 and PA-1* have the common topological feature, i.e., four big solid blocks connected through multiple narrow slender rods. However, the PT-1 with the larger w_0 supports four small solid blocks in the center. As a result, the larger δ of PA-1 shows that PA-1 is closer to water than PA-1*. Similarly, PA-2 and PA-2* have six big solid blocks in the corner and six blocks in the center. These blocks are connected with each other by the narrow connectors. PA-2 also possesses a better pentamode feature than PA-2*. Therefore, the narrower connectors generally lead to a better pentamode property and the larger objective value. To maintain the sufficient strength of the microstructure and the convergence of optimization, however, the minimal connection width is restricted to $a/60$ for the other considered microstructures throughout the present paper. Compared with the traditional honeycomb-lattice microstructures (Layman et al., 2013; Hladky-Hennion et al., 2013; Zhao et al., 2017; Su et al., 2017; Chen et al., 2017; Sun et al., 2019), these microstructures in Fig. A1 with the multiple local characteristics can possess the more tuning parameters for achieving the pentamode feature.

The effective parameters of PA-1 are $\rho^{eff} = 1010\ \mathrm{kg/m^3}$, $K_x^{eff} = K_y^{eff} = 2.36$ GPa, $K_{xy}^{eff} = 2.33$ GPa and $G_{xy}^{eff} = 0.038$ GPa. In view of the fixed mesh in optimization, PA-1 is considered to be close to water. Its dispersion relation in Fig. A1(c) shows that its longitudinal phase velocity can perfectly match with that of water within a broadband range [0, 16 kHz], while exhibiting the obvious low-order and high-order rotational modes. Nevertheless, the triangle-lattice PA-2 shows a better pentamode feature, i.e., $\rho^{eff} = 1005\ \mathrm{kg/m^3}$, $K_x^{eff} = K_y^{eff} = 2.31$ GPa, $K_{xy}^{eff} = 2.28$ GPa and $G_{xy}^{eff} = 0.0103$ GPa. Its dispersion relation in Fig. A1(f) shows that it can be perfectly matched with water in the ultra-broadband range [0, 20 kHz]. Although PA-2 can support the single-mode wave motion in the low-frequency range, it also inevitably possesses the low-order rotational mode within the broadband range.

From the viewpoint of structural configuration, the microstructures in Fig. A1 possess the multiple local characteristics and provide the novel structural foundation for PMs. But this is not sufficient for the practical application using the pentamode properties. In fact, the single-mode property can remarkably suppress the effects of the other wave modes on the underwater acoustic control, which cannot be addressed by the simple optimization model in Eq. (A1).

References

Achenbach, J., 2012. Wave Propagation in Elastic Solids. Elsevier.
Amendola, A., Smith, C.J., Goodall, R., Auricchio, F., Feo, L., Benzoni, G., Fraternali, F., 2016. Experimental response of additively manufactured metallic pentamode materials confined between stiffening plates. Compos. Struct. 142, 254–262.
Bückmann, T., Thiel, M., Kadic, M., Schittny, R., Wegener, M., 2014. An elasto-mechanical unfeelability cloak made of pentamode metamaterials. *Nat. Commun.* 5, 1–6.
Bendsoe, M.P., Sigmund, O., 2013. Topology Optimization: Theory, Methods, and Applications. Springer Science & Business Media.
Cummer, S.A., Christensen, J., Alù, A., 2016. Controlling sound with acoustic metamaterials. Nat. Rev. Mater. 1, 1–13.
Coulais, C., Sounas, D., Alù, A., 2017. Static non-reciprocity in mechanical metamaterials. Nature 542, 461–464.
Chen, Y., Liu, X., Hu, G., 2015. Latticed pentamode acoustic cloak. Sci. Rep. 5, 15745.
Chen, Y., Zheng, M., Liu, X., Bi, Y., Sun, Z., Xiang, P., Yang, J., Hu, G., 2017. Broadband solid cloak for underwater acoustics. Phys. Rev. B 95, 180104.
Chen, J., Liu, J., Liu, X., 2018. Broadband underwater acoustic carpet cloak based on pentamode materials under normal incidence. AIP Adv. 8, 085024.
Chen, Y., Hu, G., 2019. Broadband and high-transmission metasurface for converting underwater cylindrical waves to plane waves. Phys. Rev. Appl. 12, 044046.
Chu, Y., Wang, Z., Xu, Z., 2020. Broadband high-efficiency controllable asymmetric propagation by pentamode acoustic metasurface. Phys. Lett. A 384, 126230.
Cai, X., Wang, L., Zhao, Z., Zhao, A., Zhang, X., Wu, T., Chen, H., 2016. The mechanical and acoustic properties of two-dimensional pentamode metamaterials with different structural parameters. Appl. Phys. Lett. 109, 131904.
Cai, C., Guo, R., Wang, X., Sun, F., Wang, Z., Xu, Z., 2020. Effect of anisotropy on phononic band structure and figure of merit of pentamode metamaterials. J. Appl. Phys. 127, 124903.
Cheng, Y., Zhou, C., Yuan, B.G., Wu, D.J., Wei, Q., Liu, X.J., 2015. Ultra-sparse metasurface for high reflection of low-frequency sound based on artificial Mie resonances. *Nat. Mater.* 14, 1013.
Davis, B.L., Mahmoud, I.H., 2014. Nanophononic metamaterial: thermal conductivity reduction by local resonance. Phys. Rev. Lett. 112, 055505.

Dong, H.W., Wang, Y.S., Ma, T.X., Su, X.X., 2014. Topology optimization of simultaneous photonic and phononic bandgaps and highly effective phoxonic cavity. J. Opt. Soc. Am. B 31, 2946–2955.
Dong, H.W., Zhao, S.D., Wang, Y.S., Zhang, C., 2018. Broadband single-phase hyperbolic elastic metamaterials for super-resolution imaging. Sci. Rep. 8, 2247.
Dong, H.W., Zhao, S.D., Wang, Y.S., Zhang, C., 2017. Topology optimization of anisotropic broadband double-negative elastic metamaterials. J. Mech. Phys. Solids 105, 54–80.
Dong, H.W., Zhao, S.D., Wei, P., Cheng, L., Wang, Y.S., Zhang, C., 2019. Systematic design and realization of double-negative acoustic metamaterials by topology optimization. Acta Mater. 172, 102–120.
Dong, H.W., Zhao, S.D., Wang, Y.S., Cheng, L., Zhang, C., 2020. Robust 2D/3D multi-polar acoustic metamaterials with broadband double negativity. J. Mech. Phys. Solids 137, 103889.
Fang, N., Xi, D., Xu, J., Ambati, M., Srituravanich, W., Sun, C., Zhang, X., 2006. Ultrasonic metamaterials with negative modulus. *Nat. Mater.* 5, 452–456.
Frenzel, T., Kadic, M., Wegener, M., 2017. Three-dimensional mechanical metamaterials with a twist. Science 358, 1072–1074.
Fraternali, F., Amendola, A., 2017. Mechanical modeling of innovative metamaterials alternating pentamode lattices and confinement plates. J. Mech. Phys. Solids 99, 259–271.
Guo, Y., Dekorsy, T., Hettich, M., 2017. Topological guiding of elastic waves in phononic metamaterials based on 2D pentamode structures. Sci. Rep. 7, 1–7.
Gao, B., Yu, G.L., Li, J.B., 2010. Numerical simulation and experimental study on two-dimensional solid/fluid phononic crystals. J. Synth. Cryst 39, 680–686.
Guo, X., Zhang, W., Zhong, W., 2014. Doing topology optimization explicitly and geometrically: a new moving morphable components based framework. J. Appl. Mech. 81, 081009.
Hladky-Hennion, A.C., Vasseur, J.O., Haw, G., Croeenne, C., Haumesser, L., Norris, A.N., 2013. Negative refraction of acoustic waves using a foam-like metallic structure. Appl. Phys. Lett. 102, 144103.
Holland, J.H., 1975. Adaptation in Natural and Artificial Systems. University of Michigan Press, Ann Arbor.
Jahani, S., Jacob, Z., 2016. All-dielectric metamaterials. Nat. Nanotech. 11, 23–36.
Kadic, M., Bückmann, T., Stenger, N., Thiel, M., Wegener, M., 2012. On the practicability of pentamode mechanical metamaterials. Appl. Phys. Lett. 100, 191901.
Kadic, M., Bückmann, T., Schittny, R., Wegener, M., 2013. On anisotropic versions of three-dimensional pentamode metamaterials. New J. Phys. 15 (2), 023029.
Krushynska, A.O., Galich, P., Bosia, F., Pugno, N.M., Rudykh, S., 2018. Hybrid metamaterials combining pentamode lattices and phononic plates. Appl. Phys. Lett. 113, 201901.
Kadic, M., Bückmann, T., Schittny, R., Gumbsch, P., Wegener, M., 2014. Pentamode metamaterials with independently tailored bulk modulus and mass density. Phys. Rev. Appl. 2, 054007.
Kirkpatrick, S., Gelatt, C.D., Vecchi, M.P., 1983. Optimization by simulated annealing. Science 220, 671–680.
Liu, Z., Zhang, X., Mao, Y., Zhu, Y.Y., Yang, Z., Chan, C.T., Sheng, P., 2000. Locally resonant sonic materials. Science 289, 1734–1736.
Lai, Y., Wu, Y., Sheng, P., Zhang, Z.Q., 2011. Hybrid elastic solids. *Nat. Mater.* 10, 620–624.
Liu, X., Tyler, T., Starr, T., Starr, A.F., Jokerst, N.M., Padilla, W.J., 2011. Taming the blackbody with infrared metamaterials as selective thermal emitters. Phys. Rev. Lett. 107, 045901.
Li, Y., Zhu, K.J., Peng, Y.G., Li, W., Yang, T., Xu, H.X., Chen, H., Zhu, X.F., Fan, S., Qiu, C.W., 2019. Thermal meta-device in analogue of zero-index photonics. Nat. Mater. 18, 48–54.
Li, Y., Kita, S., Muñoz, P., Reshef, O., Vulis, D.I., Yin, M., Lončar, M., Mazur, E., 2015. On-chip zero-index metamaterials. Nat. Photon. 9, 738–742.
Liang, Z., Li, J., 2012. Extreme acoustic metamaterial by coiling up space. Phys. Rev. Lett. 108, 114301.
Layman, C.N., Naify, C.J., Martin, T.P., Calvo, D.C., Orris, G.J., 2013. Highly anisotropic elements for acoustic pentamode applications. Phys. Rev. Lett. 111, 024302.
Liu, X.N., Hu, G.K., Huang, G.L., Sun, C.T., 2011a. An elastic metamaterial with simultaneously negative mass density and bulk modulus. Appl. Phys. Lett. 98, 251907.
Liu, X.N., Hu, G.K., Sun, C.T., Huang, G.L., 2011b. Wave propagation characterization and design of two-dimensional elastic chiral metacomposite. J. Sound Vib. 330, 2536–2553.
Li, J., Shen, C., Díaz-Rubio, A., Tretyakov, S.A., Cummer, S.A., 2018. Systematic design and experimental demonstration of bianisotropic metasurfaces for scattering-free manipulation of acoustic wavefronts. Nature Commun. 9, 1342.
Moitra, P., Yang, Y., Anderson, Z., Kravchenko, I.I., Briggs, D.P., Valentine, J., 2013. Realization of an all-dielectric zero-index optical metamaterial. Nat. Photon. 7, 791–795.
Milton, G.W., Cherkaev, A.V., 1995. Which elasticity tensors are realizable? J. Eng. Technol. 117, 483–493.
Martin, A., Kadic, M., Schittny, R., Bückmann, T., Wegener, M., 2012. Phonon band structures of three-dimensional pentamode metamaterials. Phys. Rev. B 86, 155116.
Michie, D., Spiegelhalter, D.J., Taylor, C.C., 1994. Machine learning. Neural Stat. Classif. 13, 1–298.
Molerón, M., Serra-Garcia, M., Daraio, C., 2016. Visco-thermal effects in acoustic metamaterials: from total transmission to total reflection and high absorption. New J. Phys. 18, 033003.
Nguyen, V.C., Chen, L., Halterman, K., 2010. Total transmission and total reflection by zero index metamaterials with defects. Phys. Rev. Lett. 105, 233908.
Norris, A.N., 2014. Mechanics of elastic networks. P. Roy. Soc. A-Math. Phy. 470, 20140522.
Pendry, J.B., 2000. Negative refraction makes a perfect lens. *Phys. Rev. Lett.* 85, 3966.
Poddubny, A., Iorsh, I., Belov, P., Kivshar, Y., 2013. Hyperbolic metamaterials. Nat. Photon. 7, 948–957.
Podestá, J.M., Méndez, C.M., Toro, S., Huespe, A.E., 2019. Symmetry considerations for topology design in the elastic inverse homogenization problem. J. Mech. Phys. Solids 128, 54–78.
Smith, D.R., Pendry, J.B., Wiltshire, M.C., 2004. Metamaterials and negative refractive index. Science 305, 788–792.
Shalaev, V.M., 2007. Optical negative-index metamaterials. Nat. Photon. 1, 41–48.
Shen, C., Xie, Y., Sui, N., Wang, W., Cummer, S.A., Jing, Y., 2015. Broadband acoustic hyperbolic metamaterial. Phys. Rev. Lett. 115, 254301.
Sun, Z., Sun, X., Jia, H., Bi, Y., Yang, J., 2019. Quasi-isotropic underwater acoustic carpet cloak based on latticed pentamode metafluid. Appl. Phys. Lett. 114, 094101.
Schittny, R., Bückmann, T., Kadic, M., Wegener, M., 2013. Elastic measurements on macroscopic three-dimensional pentamode metamaterials. Appl. Phys. Lett. 103, 231905.
Su, X., Norris, A.N., Cushing, C.W., Haberman, M.R., Wilson, P.S., 2017. Broadband focusing of underwater sound using a transparent pentamode lens. J. Acoust. Soc. Am. 141, 4408–4417.
Sun, Z., Jia, H., Chen, Y., Wang, Z., Yang, J., 2018. Design of an underwater acoustic bend by pentamode metafluid. J. Acoust. Soc. Am. 143, 1029–1034.
Scandrett, C.L., Boisvert, J.E., Howarth, T.R., 2011. Broadband optimization of a pentamode-layered spherical acoustic waveguide. Wave Motion 48, 505–514.
Tian, Y., Wei, Q., Cheng, Y., Xu, Z., Liu, X., 2015. Broadband manipulation of acoustic wavefronts by pentamode metasurface. Appl. Phys. Lett. 107, 221906.
Wu, Y., Lai, Y., Zhang, Z.Q., 2011. Elastic metamaterials with simultaneously negative effective shear modulus and mass density. *Phys. Rev. Lett.* 107, 105506.
Wang, M.Y., Wang, X., Guo, D., 2003. A level set method for structural topology optimization. *Comput. Method. Appl. M.* 192, 227–246.
Wang, P., Casadei, F., Shan, S., Weaver, J.C., Bertoldi, K., 2014. Topology optimization of simultaneous photonic and phononic bandgaps and highly effective phoxonic cavity. *Phys. Rev. Lett.* 113, 014301.
Xie, Y.M., Steven, G.P., 1993. A simple evolutionary procedure for structural optimization. Comput. Struct. 49, 885–896.
Yang, M., Ma, G., Yang, Z., Sheng, P., 2013. Coupled membranes with doubly negative mass density and bulk modulus. Phys. Rev. Lett. 110, 134301.
Zheludev, N.I., Kivshar, Y.S., 2012. From metamaterials to metadevices. *Nat. Mater.* 11, 917–924.

Zhu, R., Liu, X.N., Hu, G.K., Sun, C.T., Huang, G.L., 2014. Negative refraction of elastic waves at the deep-subwavelength scale in a single-phase metamaterial. *Nat. Commun.* 5, 1–8.
Zhao, A., Zhao, Z., Zhang, X., Cai, X., Wang, L., Wu, T., Chen, H., 2017. Design and experimental verification of a water-like pentamode material. Appl. Phys. Lett. 110, 011907.
Zheng, M., Liu, X., Chen, Y., Miao, H., Zhu, R., Hu, G., 2019. Theory and realization of nonresonant anisotropic singly polarized solids carrying only shear waves. Phys. Rev. Appl. 12, 014027.